

Design Rules for Optimizing Quaternary Mixed-Metal Chalcohalides

Pascal Henkel

*Department of Applied Physics, Aalto University,
P.O.Box 11100, FI-00076 AALTO, Finland*

Jingrui Li

*State Key Laboratory for Manufacturing Systems
Engineering; Electronic Materials Research Laboratory,
Key Laboratory of the Ministry of Education,
School of Electronic Science and Engineering; International Joint
Laboratory for Micro/Nano Manufacturing and Measurement Technology,
Xi'an Jiaotong University, Xi'an 710049, China*

Patrick Rinke

*Physics Department, Technical University of Munich, Garching, Germany
Atomistic Modelling Center, Munich Data Science Institute,
Technical University of Munich, Garching, Germany
Munich Center for Machine Learning (MCML) and
Department of Applied Physics, Aalto University,
P.O.Box 11100, FI-00076 AALTO, Finland*

(Dated: November 20, 2025)

Abstract

Quaternary mixed-metal $M(II)_2M(III)Ch_2X_3$ chalcohalides are an emerging material class for photovoltaic absorbers that combines the beneficial optoelectronic properties of lead-based halide perovskites with the stability of metal chalcogenides. Inspired by the recent discovery of lead-free mixed-metal chalcohalides materials, we utilized a combination of density functional theory and machine learning to determine compositional trends and chemical design rules in the lead-free and lead-based materials spaces. We explored a total of 54 $M(II)_2M(III)Ch_2X_3$ materials with $M(II) = Sn, Pb$, $M(III) = In, Sb, Bi$, $Ch = S, Se, Te$, and $X = Cl, Br, I$ per phase ($Cmcm$, $Cmc2_1$, and $P2_1/c$). The $P2_1/c$ phase is the equilibrium phase at low temperatures, followed by $Cmc2_1$ and $Cmcm$. The fundamental band gaps in $Cmcm$ and $Cmc2_1$ are smaller than those in $P2_1/c$, but direct band gaps are more common in $Cmcm$ and $Cmc2_1$. The effective electron masses in $P2_1/c$ are significantly larger compared to $Cmcm$ and $Cmc2_1$, while the effective hole masses are nearly the same across all three phases. Using random forest regression, we found that the two electron acceptor sites (Ch and X) are crucial in shaping the properties of mixed-metal chalcohalide compounds. Furthermore, the electron donor sites ($M(II)$ and $M(III)$) can be used to finetune the material properties to desired applications. These design rules enable precise tailoring of mixed-metal chalcohalide compounds for a variety of applications.

I. INTRODUCTION

Photovoltaic (PV) technologies are ideal for providing clean, affordable, and secure energy, facilitating a shift towards sustainable energy production. Continuous development of new PV materials is essential to enhance power conversion efficiency (PCE), extend device longevity, and reduce costs, thereby promoting the widespread adoption of solar cells. Metal halide perovskites have emerged as promising candidates.[1–3] Specifically, lead halide perovskites (LHPs) offer cost-effective fabrication, advantageous optoelectronic properties, and high defect tolerance.[4–6] However, the commercial viability of LHPs is challenged by lead toxicity and their moderate long-term stability in air.[5, 7–9] Low toxicity alternatives to LHPs include Sn^{2+} -, Sb^{3+} - or Bi^{3+} -based perovskites. However, these materials face challenges such as high defect densities and oxidation in air (Sn^{2+} to Sn^{4+}).[10] Metal chalcogenides based on Pb^{2+} , Cd^{2+} , or Sb^{3+} [11–14] have emerged as promising LHP alternatives

due to their high absorption cross sections and tunable band gaps. Stable solar cells have already been demonstrated for these materials, albeit with modest efficiencies.[3, 11, 13, 15]

Perovskite-inspired quaternary mixed-metal chalcohalides (MMCHs) that combine halide perovskite (ABX_3) and metal chalcogenide (MCh_2) building blocks are a promising semiconductor material class for photovoltaic applications.[16–18] Their stoichiometry is $M(II)_2M(III)Ch_2X_3$ (or $A_2BCh_2X_3$ in short)[17] where the $M(II)$ - and $M(III)$ -sites are occupied by metals with ns^2 lone pair electron(s), the Ch -site by chalcogens, and the X -site by halogens. The properties of both building blocks may combine synergistically in mixed-metal chalcohalides as evidenced by a high defect tolerance owing to the strong dielectric screening (due to ns^2 lone pair electrons), the resultant low capture cross-sections of defects, and dispersive valence and conduction band edges.[7, 8, 16] Also, the strong metal-chalcogen bond, which is formed in MMCH materials between the bivalent chalcogenide anions and both $M(II)$ and $M(III)$ metal cations, can overcome the known stability challenges of LHPs.[5, 16] In addition, the strength of the Sn - Ch bond should prevent the oxidation from Sn^{2+} to Sn^{4+} in lead-free MMCH-based compounds. As a result, $Sn_2M(III)Ch_2X_3$ films can be stable in humid conditions when synthesized under reduction conditions, as verified by experimental X-ray photoelectron spectroscopy.[16, 17] Recently, Nie *et al.* achieved a PCE of 4.04 % for a $Sn_2SbS_2I_3$ -based single-junction solar cell,[16] which highlights the PV potential of mixed-metal chalcohalides. 4.04 % is a promising start considering that perovskite solar cells initially showed a PCE of 3.8 % in 2009[19] and now exceed 26 %. [3]

In this work, we focus on the MMCH materials space and apply density functional theory (DFT) and machine learning to assess its potential for PV applications. Recently, we explored solely the lead-free MMCH materials with DFT and discovered 24 new materials[20] bringing the total up to 27 (including the already known $Sn_2SbS_2I_3$,[16, 17, 21–23] $Sn_2SbSe_2I_3$,[24] and $Sn_2BiS_2I_3$ [25]) compounds. Now we extend our study to the lead-based $Pb_2M(III)Ch_2X_3$ materials space, reporting 25 previously unstudied compounds alongside the two known materials, $Pb_2SbS_2I_3$ [26–28] and $Pb_2BiS_2I_3$,[25, 28] which had been the only Pb-based representatives reported to date. We compute the equilibrium properties of the 27 lead-based counterparts to the tin compounds of our previous study with DFT. We then apply a random forest (RF) machine learning model and the Shapley additive explanations (SHAP) analysis to discover chemical trends for lead-free as well as lead-based perovskite-inspired quaternary mixed-metal chalcohalides.

Our goal is to go beyond a purely DFT-based analysis by leveraging a combination of RF models and SHAP analysis to identify and understand the root of chemical trends of the four atomic sites and their elements on material properties for a total of 54 lead-free and lead-based MMCH compounds. To cover a broad range of MMCH materials, we considered Sn^{2+} and Pb^{2+} (both with ns^2 lone pair electrons) for the M(II)-site, and Sb^{3+} , Bi^{3+} (both with ns^2 lone pair electrons), and In(III) (with a $5d^{10}6s^0$ valence electron configuration) for the M(III)-site. Additionally, we included S^{2-} , Se^{2-} , and Te^{2-} for the Ch-site, and Cl^- , Br^- , and I^- for the X-site. We considered three phases (Cmcm , $\text{Cmc}2_1$, and $\text{P}2_1/\text{c}$) in which MMCH materials can crystallize to ensure structural diversity. This allows us to assess the dominance of electron acceptor sites (Ch and X) over electron donor sites (M(II) and M(III)). An additional objective is to determine whether and how the chemical trends depend on the material parameters, such as the consistent decrease in formation energies (thermodynamic stabilities), band gaps, as well as effective electron and hole masses from Cl via Br to I. Finally, we will investigate the effect of the MMCH structure and phase on the chemical trends.

The structure of this article is as follows: In Section II, we outline our computational workflow, starting with data generation using DFT, followed by the creation of appropriate RF models to examine the influence of atomic sites, and concluding with an analysis of the elements' impact on material properties using SHAP. Section III reports the effects of atomic sites and elements on material properties. Section IV discusses the identified effects and design rules on one hand within the MMCH materials space and on the other hand in terms of chemical origin. Finally, Section V provides a summary of our findings.

II. MODELS AND COMPUTATIONAL DETAILS

We used a combination of different methods to study trends in the MMCH materials space. Here we describe how we calculated the material properties (formation energy, fundamental band gap, optical band gap, and effective electron and hole masses) for different MMCHs crystal structures by means of DFT. Next, we outline how we determined the influence of atomic sites (M(II), M(III), Ch and X) on the materials properties with RF regression models. Finally, we present details of the SHAP analysis to assess the impact of different elemental substitutions on the materials properties.

A. $M(II)_2M(III)Ch_2X_3$ structures

The structural framework of $M(II)_2M(III)Ch_2X_3$ materials consists of four distinct atomic sites (see Figure 1): the two metal sites $M(II)$ and $M(III)$, the chalcogen site Ch , and the halogen site X . Both metal sites are occupied by ns^2 lone pair metals, except In for $M(III)$, serving as electron donors, while the Ch - and X -sites function as electron acceptors.

MMCH materials can crystallize, as revealed by X-ray diffraction measurements and DFT calculations, in three different phases: $Cmcm$ (#63), $Cmc2_1$ (#36), and $P2_1/c$ (#14),[17, 20–28] see Figure 1. Throughout the manuscript, the three MMCH structures are distinguished by their respective space group labels. The orthorhombic $Cmcm$ phase is prevalent at room temperature,[21, 24–28] and transitions to a monoclinic $P2_1/c$ phase below 100 K, as demonstrated by Doussier *et al.* for $Pb_2SbS_2I_3$.[27] DFT calculations for $Sn_2SbS_2I_3$ suggest that the $Cmcm$ structure, is thermodynamically unstable at 0 K due to imaginary phonon modes, can be viewed as an average of the more energetically favorable, lower symmetry $Cmc2_1$ phase.[17] Ab-initio molecular dynamic simulations further demonstrated a transition from $Cmcm$ to $Cmc2_1$ phase at 500 K,[17] highlighting the entropic stabilization effect of the $Cmcm$ phase. Additionally, the $P2_1/c$ phase is energetically favorable over $Cmcm$ and $Cmc2_1$.[22] A more detailed description of the structural characteristics of MMCH materials crystallizing in the three phases ($Cmcm$, $Cmc2_1$ and $P2_1/c$) is given in Section SM 1 in the Supplemental Material (SM).[29]

The initial structures for all MMCHs have been generated based on known materials listed in the Materials Project.[30] For the $Cmcm$ and $Cmc2_1$ phases we used the corresponding $Sn_2SbS_2I_3$ structures (ref. numbers: mp-561134 and mp-1219046) and for $P2_1/c$ phases the corresponding $Pb_2SbS_2I_3$ structure (ref. number: mp-578882). We carried out substitutions on the $M(II)$ -, $M(III)$ -, Ch -, and X -sites to generate a total of 54 MMCHs per phase.

B. Density functional theory calculations

We determined the material properties (formation energy, fundamental band gaps, optical gaps, effective electron and hole masses) of all 54 MMCHs in the three phases for our RF-based analysis with DFT. We performed spin unpolarized DFT calculations with the all-electron, numeric atom-centered orbital code FHI-aims.[32–37] We chose the Perdew-



M(II)= Sn, Pb



M(III) = In, Sb, Bi



Ch = S, Se, Te



X = Cl, Br, I

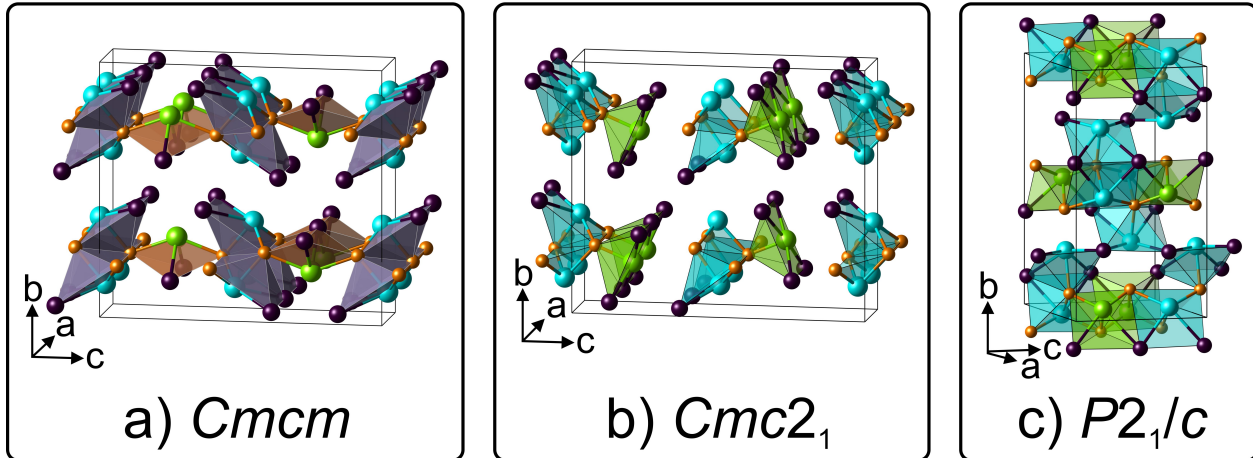


Figure 1. Illustration of different phases; a) $Cmcm$, b) $Cmc2_1$, and c) $P2_1/c$ in MMCH structures. The respective M(II) coordination polyhedrons are depicted in cyan and the M(III) coordination polyhedrons in green. The coordinates of each phase were taken from the Materials Project[30] and were visualized with VESTA.[31]

Burke-Ernzerhof exchange-correlation functional for solids (PBEsol) [38, 39] due to its computational efficiency and its good agreement with experimental lattice constants for various halide perovskites[40–44] and the five known MMCHs. On average, PBEsol underestimates the lattice constants for the known MMCHs by $\sim 1.7\%$ for $Cmcm$, $\sim 1.6\%$ for $Cmcm$ and $\sim 0.4\%$ for $P2_1/c$. Atomic geometries were relaxed with the Broyden-Fletcher-Goldfarb-Shanno algorithm[45] in two steps. We first pre-optimized each structure with *light* real-space grid settings and a tier-1 basis and then refined the geometry using *tight* settings and a tier-2 basis. The structures were relaxed until all forces acting on the atoms were smaller than $5 \times 10^{-3} \text{ eV } \text{\AA}^{-1}$. The electronic self-consistency convergence threshold was set to $1 \times 10^{-6} \text{ eV}$. A Gaussian broadening of 0.01 eV was applied to all electronic occupations and relativistic effects were included based on the zero-order regular approximation.[32, 46] In addition to PBEsol geometry optimization, we performed single point calculations for the band structures, the absorption spectra and the density of state (DOS) with the range-separated hybrid Heyd-Scuseria-Ernzerhof (HSE06) functional (with 25 % exact exchange)[47–49] including spin-orbit coupling[50] and a tier-2 basis. The effective masses were extracted from the band structure with a quadratic least-squares fit to the respective band edges assuming a

parabolic dispersion with the implementation of Whalley in the *effmass* package[51]. In addition, the absorption spectra were calculated based on the linear macroscopic dielectric tensor[52] within the independent particle approximation.

We used 16-atom unit cells for the *Cmcm* (#63) (see Figure 1a) and *Cmc2₁* (#36) (see Figure 1b) phases and a 32-atom unit cell for the *P2₁/c* (#14) (see Figure 1c)) phase. For PBEsol geometry optimization, we sampled the Brillouin zone with a Γ -centered $11 \times 11 \times 3$ k -point mesh for the *Cmcm* and *Cmc2₁* phases and $6 \times 3 \times 5$ for *P2₁/c*. For the HSE06 band structure and absorption spectra calculations, we increased the grids to Γ -centered $16 \times 16 \times 4$ for *Cmcm* and *Cmc2₁* and $9 \times 4 \times 8$ for *P2₁/c*.

The complex nature of MMCH compounds makes a rigorous stability analysis highly demanding, as it requires knowledge of all competing phases within the quaternary phase space. As a computationally feasible DFT-based approximation, we estimate the thermodynamic stability (at 0 K) by calculating the formation energy with respect to elemental decomposition of an individual MMCH compound as

$$E_{\text{form}}[\text{M(II)}_2\text{M(III)}\text{Ch}_2\text{X}_3] = E_{\text{tot}}[\text{M(II)}_2\text{M(III)}\text{Ch}_2\text{X}_3] - \sum_i x_i \mu_i. \quad (1)$$

$E_{\text{tot}}[\text{M(II)}_2\text{M(III)}\text{Ch}_2\text{X}_3]$ is the total energy of $\text{M(II)}_2\text{M(III)}\text{Ch}_2\text{X}_3$, x_i the number of atoms of the i th element, and μ_i the corresponding chemical potential. The upper limit for the chemical potential is given by $\mu_i \leq E_{\text{tot}}(i\text{th element})$, i.e., the total energy per atom in the most stable pure phase.[53] We used the following elemental compounds with the same computational parameters but adjusted Γ -centered k -point meshes: Sn *I4₁/amd* (#141), Pb *Fm\bar{3}m* (#225), In *I4/mmm* (#139), Sb *R\bar{3}m* (#166), Bi *R\bar{3}m* (#166), S *Fddd* (#70), Se *P2₁/c* (#14), and Te *P3₁21* (#152), as well as Cl, Br, and I in the gas phase as X_2 .

In the interest of open materials science[54] we make all relevant data publicly available; see reference 55 for lead-free and 56 for lead-based $\text{M(II)}_2\text{M(III)}\text{Ch}_2\text{X}_3$ materials.

C. Random forest regression modeling

We used RF regression of the DFT data as a means to determine the impact of each atomic site (M(II), M(III), Ch, and X) on different material properties. RF is a non-linear and non-parametric ensemble learning method composed of different decision trees.[57] For regression models, as used in this study, the predicted target is averaged over the individual

decision trees, which increases prediction accuracy and reduces overfitting.[58]

For each phase, we first created a data set that contains the material properties for each MMCH material. As a descriptor we use the atomic numbers of all elements within each MMCH, e.g., $\text{Sn}_2\text{SbS}_2\text{I}_3$ is represented by the array [50, 51, 16, 53]. Next, we trained an RF regression model for each material property using the atomic numbers as input and the respective material property as the target value. To determine the optimal RF hyperparameters, we used the cross-validated grid-search (*GridSearchCV*) method implemented in *scikit-learn*.[59] A 75 %/25 % split for the training/test data was used to determine the performance of each hyperparameter combination. The mean absolute error (MAE) and root mean square error between predicted and DFT-calculated material properties are calculated for each hyperparameter set to assess the performance. In addition, a 10-fold cross validation was carried out to ensure the robustness of each hyperparameter set. The best performing hyperparameter set is applied to analyze the entire data set. The performance of the RF models for the formation energy, (fundamental) band gap, effective electron and hole masses for different phases is presented in Figure SM 1. In addition, we also trained RF models for the lowest direct band gaps and optical band gaps, see Figures SM 2 and SM 3 for their individual performance. We used the final trained RF models to determine the importance of the atomic sites for each material property. Each atomic site is one feature of our input space and we used the built-in feature importance tools of *scikit-learn*.

Additionally, we also tested other descriptors such as electro-negativity (EN), electron affinity (EA), ionization energy (IE) as well as atomic, Van der Waals, and covalent radii. In the past, descriptors based on such tabulated properties have been successfully used to predict material properties for a variety of material systems, such as N-based semiconductors,[60] ABX_3 ,[61] and $\text{A}'\text{A}''\text{B}'\text{B}''\text{X}_6$ double perovskites.[62] Gladkikh *et al.* and Pilania *et al.* used such element-derived descriptors in combination with kernel ridge regression model to predict the band gaps of ABX_3 [61] and $\text{A}'\text{A}''\text{B}'\text{B}''\text{X}_6$ double perovskites.[62] However, we found for MMCH materials that the atomic numbers provided the best performance. Furthermore, we tested the sure independence screening and sparsifying operator (SISSO) approach as implemented in *SISSO++*,[63] but the results were not as good as those of the RF.

D. Shapley additive explanations analysis

To examine the impact of elements on material properties within the MMCH materials space, we analyzed the resulting RF models using the SHAP method.[64] SHAP, based on game theory and an additive feature attribution approach, explains machine learning outputs. Its purpose is to identify the contribution (SHAP value) of each feature (in our case of each element within a MMCH compound) to the predicted target value. Various methods can approximate SHAP values. We here use *TreeSHAP*, specifically designed for RFs [65, 66], to assess the influence of the features (atomic numbers of elements within the four atom sites of MMCH compounds) on the material parameters. For each RF model, a SHAP base value is first determined, representing the mean of the predicted values. Then, the contribution of each feature to the predicted target value is calculated relative to the SHAP base value. In this study, we use the SHAP implementation by Lundberg.[67]

In this study, we exclusively use the mean SHAP values for each element type to enhance interpretability. Since the contribution of each element varies depending on the specific MMCH compound, minor deviations in element type contributions are observed. For instance, the SHAP contribution of Cl to the formation energy is -75 meV in $\text{Sn}_2\text{SbS}_2\text{Cl}_3$ and -77 meV in $\text{Sn}_2\text{BiTe}_2\text{Cl}_3$. Therefore, we report the mean SHAP contribution along with the corresponding variance, which characterizes the distribution around the mean value.

III. RESULTS

We examine the impact of atomic sites and elements on the formation energy, fundamental band gap, and effective electron and hole masses of MMCH materials in their *Cmcm* phase. This analysis allows us to identify material property trends across the MMCH materials space. The results for the *Cmc2*₁ and *P2*₁/*c* phases are shown in Figures SM 4 and SM 5 for the formation energy, Figures SM 6 and SM 7 for the fundamental band gap, and Figures SM 14, SM 16, SM 15, and SM 17 for the effective masses of electrons and holes. Additionally, Table SM I lists all material parameters for all 54 MMCH materials across all phases.

A. Formation energies

We have previously determined that lead-free MMCH materials are stable with respect to elemental decomposition.[20] Here we show that this stability also extends to the lead-based counterparts as evidenced by their negative formation energies, listed in Table SM I. Therefore, all 54 MMCH materials are stable - independent of their phase. We observe that the $P2_1/c$ phase is most prevalent (i.e., has the highest absolute formation energies) followed by $Cmc2_1$ then $Cmcm$, see Table SM I.

Figure 2a shows the atomic site importance of the formation energy for all 54 MMCH materials in the $Cmcm$ phase as determined by the RF model. The X-site has the largest influence (50 %) followed by the Ch-site (34 %). In contrast, both M(II) (6 %) and M(III) (10 %) metal sites have only minor effects on the formation energy.

The corresponding SHAP analysis is presented in Figure 2b and offers more detail on the elemental contributions to the formation energy. SHAP reveals that Cl and Br decrease the formation energy (Cl more than Br) and I increases it. On the Ch-site, S and Se decrease the formation energy (almost by the same amount on average), while Te increases it. For Bi, In, and Pb we also observe decreases, while Sb and Sn increase the formation energy. In correspondence with the feature importance, the formation energy change caused by the metal atoms on M(II)- and M(III)-site is less than that of the X- and Ch-site elements. We observed a similar behavior for the $Cmc2_1$ and the $P2_1/c$ phases as shown correspondingly in Figures SM 4 ($Cmc2_1$) and SM 5 ($P2_1/c$) in the SM.

B. Fundamental band gaps

MMCH materials are mainly semiconductors, with the exception of $Sn_2InTe_2Br_3$ and $Sn_2BiTe_2I_3$ in the $Cmcm$ phase (see Table SM I). The majority of the computed, fundamental band gaps are indirect. Only $\sim 33\%$ of lead-free and $\sim 40\%$ of lead-based MMCH compounds feature a direct fundamental band gap in their $Cmcm$ and $Cmc2_1$ phases. Also, the vast majority of MMCH compounds in the $P2_1/c$ phase have an indirect fundamental band gap. Only $\sim 7\%$ of lead-free and $\sim 11\%$ of lead-based $M(II)_2M(III)Ch_2X_3$ compounds exhibit a direct fundamental band gap. The average values of the fundamental band gap in the $Cmcm$, $Cmc2_1$, and $P2_1/c$ phases are ~ 1.2 , ~ 1.1 , and ~ 1.6 eV, respectively.

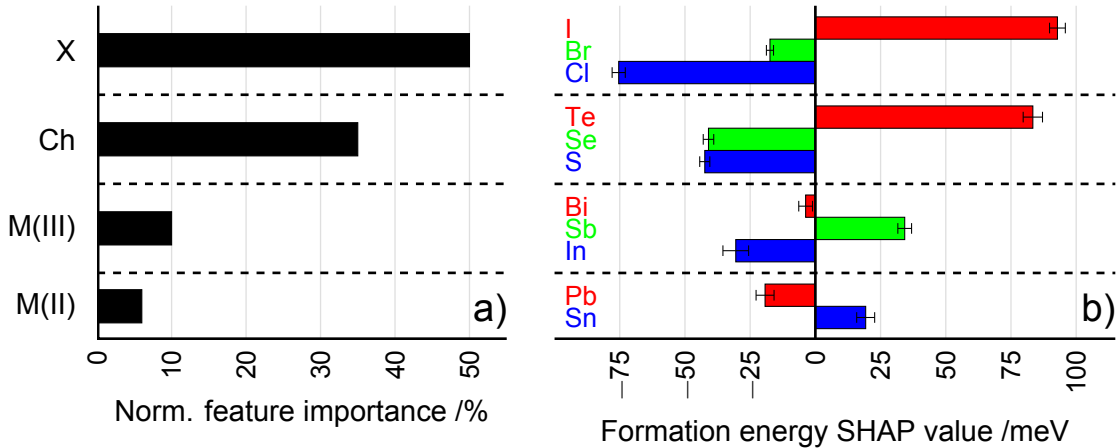


Figure 2. Summary of the feature importance of the formation energy in the RF model for the *Cmcm* phase: a) Normalized atom site importance for the predicted formation energy in percent; b) impact of elements on the M(II)-, M(III)-, Ch-, and X-sites measured in terms of their mean SHAP values on the predicted base formation energy value in meV. The error bars denote the standard deviation for each mean SHAP value. Since the formation energy is negative, negative mean SHAP values indicate a stabilization of the material and positive SHAP values a destabilization.

Figure 3a presents the same feature importance analysis done for the formation energy in the previous section now for the fundamental band gap in the *Cmcm* phase. The band gap is mainly influenced by the chalcogen site (38 %), followed by both metal sites (23 % for both M(II) and M(III); see Figure 3a). In contrast to the formation energy, halogens have the smallest (16 %) influence on the fundamental band gap. The corresponding SHAP analysis in Figure 3b reveals that on the X-site Cl and Br decrease the fundamental band gap while I increases it. Similarly, on the Ch-site S and Se increase the fundamental band gap and Te decreases it. For both metal sites, In and Pb lead to a band gap increase while Bi, Sb and Sn reduce the gap.

Again, we observed a similar behavior for the *Cmc2₁* and *P2₁/c* phases (see Figures SM 6 and SM 7, respectively). Furthermore, we obtained similar results for an RF model trained on the lowest direct band gap for each material instead of the lowest fundamental band gap (which includes a mix of direct and indirect band gaps). The results for the lowest direct band gap are presented in Figures SM 8 (*Cmcm*), SM 9 (*Cmc2₁*) and SM 10 (*P2₁/c*).

We also calculated the absorption spectra for all 54 MMCH compounds in the three

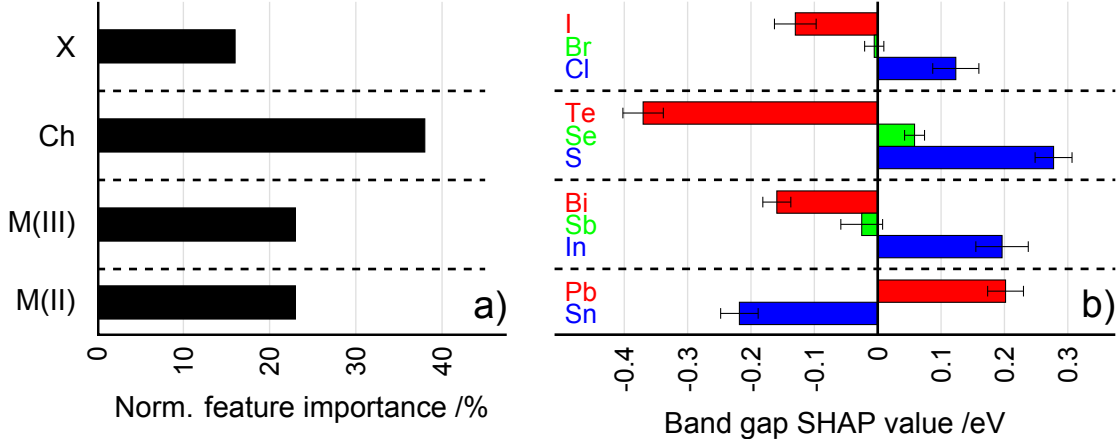


Figure 3. Summary of the feature importance of the fundamental band gap in the RF model for the *Cmcm* phase: a) Normalized atom site importance for the predicted fundamental band gap in percent; b) impact of elements on the M(II)-, M(III)-, Ch- and X-sites quantified in terms of their mean SHAP values for the predicted base fundamental band gap in eV. The error bars denote the standard deviation for each mean SHAP value.

phases in the independent particle approximation. We then determined the optical band gaps as onset of absorption from the corresponding Tauc plots. In our previous work,[20] we had demonstrated that the optical band gap lies on average 0.29 eV above the fundamental band gap for the lead-free MMCH compounds. For the lead-based systems, the difference is 0.22 eV, which drops the average for the whole MMCH materials system to 0.26 eV. Figures SM 11 (*Cmcm*), SM 12 (*Cmc2*₁) and SM 13 (*P2*₁/*c*) show the corresponding feature importance analysis for the optical band gaps for all three phases. We observe that also the optical band gap is determined by the Ch-, M(II)- and M(III)-sites.

C. Effective electron and hole masses

Table SM I also lists the effective electron and hole masses for the investigated MMCH materials. Unlike for the formation energy (Section III A) and the fundamental band gap (Section III B), the effective masses behave differently across the three different phases. For *P2*₁/*c*, the average electron ($1.42 m_0$ with $m_0 = 9.109 \times 10^{-31}$ kg denoting the free electron mass) and hole ($1.46 m_0$) masses are almost the same, while for *Cmcm* and *Cmc2*₁ electrons are lighter than holes ($m_e^{Cmcm} = 0.86 m_0$, $m_h^{Cmcm} = 1.37 m_0$, $m_e^{Cmc21} = 0.93 m_0$,

and $m_h^{Cmc21} = 1.38 m_0$).

The corresponding feature importance plots are shown in Figures 4a and 5a for *Cmcm*, Figures SM 14a and SM 16a for *Cmc21*, and SM 15a and SM 17a for *P21/c*. They reveal that the M(II)-site has the lowest impact on the effective electron and hole masses regardless of the phase. The order of importance of the other three sites varies for different phases. For the *Cmcm* phase, the X-site has the largest influence, although all three sites are closer together in their effect (between 23 % and 33 %) than they were for the formation energy and the fundamental band gap.

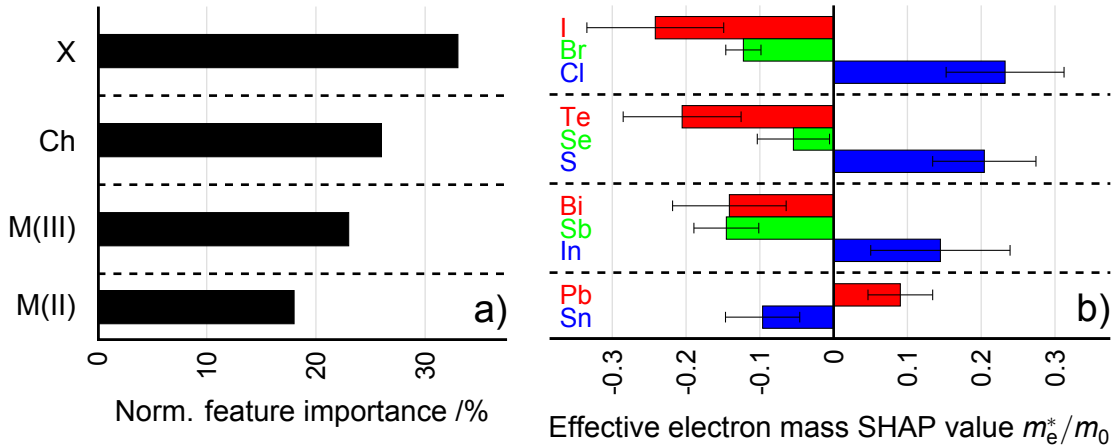


Figure 4. Summary of the feature importance of the effective electron mass in the RF model for the *Cmcm* phase: a) Normalized atom site importance for the predicted electron mass in percent; b) impact of elements on the M(II)-, M(III)-, Ch-, and X-sites quantified in terms of their mean SHAP values for the predicted base effective hole mass value per m_0 (free electron mass). The error bars denote the standard deviation for each mean SHAP value.

Our SHAP analysis (see Figures 4b and 5b for *Cmcm*) reveals that in all three phases the halogens I and Br decrease the effective electron and hole masses whereas Cl increase them. Similarly, on the M(II)-site Pb increases and Sn decreases the effective masses. For the *Cmcm* phase, also Te, Bi, and Sb have a decreasing effect, while S and In always increase both effective masses. Only Se changes its role, providing a small decrease of the electron, but a moderate increase of the hole masses. For the other two phases, these elemental effects are slightly different and are summarized in Table I as well as Figures SM 14b & SM 16b (*Cmc21*) and SM 15b & SM 17b (*P21/c*).

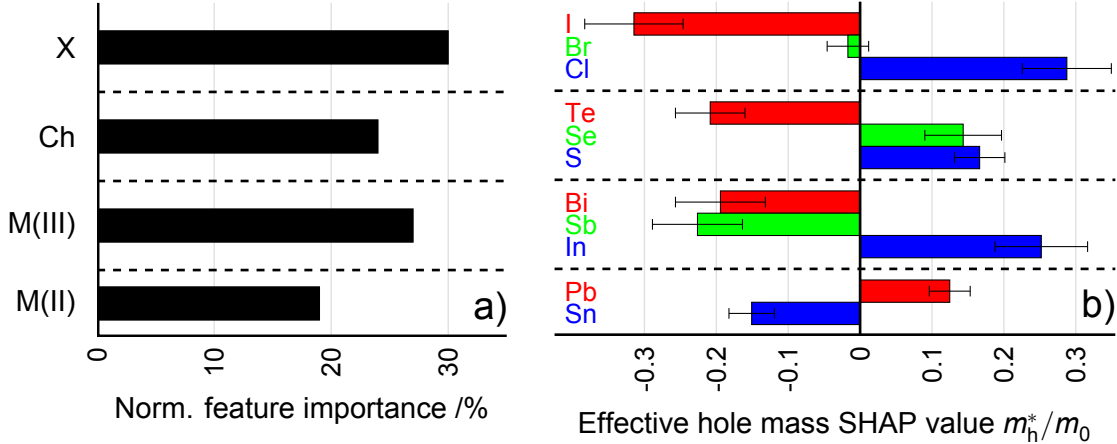


Figure 5. Summary of the feature importance of the effective hole mass in the RF model for the *Cmcm* phase: a) Normalized atom site importance for the predicted effective hole mass in percent; b) impact of elements on the M(II)-, M(III)-, Ch-, and X-sites quantified in terms of their mean SHAP values for the predicted base effective hole mass value per m_0 . The error bars denote the standard deviation for each mean SHAP value.

IV. DISCUSSION

Firstly, our analysis of the formation energy in Section III A shows that MMCH stability (which can be estimated from the formation energy, as more negative means more stable) is mainly influenced by the two electron acceptor sites (Ch and X) with the two metal sites (M(II) and M(III)) playing only a minor role, see Figure 2a. From the corresponding SHAP analysis in Figure 2b we can deduce the following trends, which could be used as materials design rules: The formation energy decreases (and thus the stability increases) for halogens on the X-site along $\text{Cl} > \text{Br} > \text{I}$ and for chalcogens on the Ch-site along $\text{S} \simeq \text{Se} > \text{Te}$. On the M(III)-site the formation energy decreases along $\text{In} > \text{Bi} > \text{Sb}$. Lastly, lead-based MMCHs are more stable than their Sn-based counterparts ($\text{Pb} > \text{Sn}$), which is in good agreement with theoretical[68] and experimental[69–71] observations for Sn- and Pb-based perovskites.

These design rules can be rationalized by the strength of the metal-halide and the metal-chalcogen bonds. The EN of the elements, i.e., the strength with which an element can attract valence electrons, can be used as an indicator for the bond strength. Since the X and Ch-site in MMCH compounds are both electron acceptors, the bond strength increases with EN, as both sites seek to attract electron density in the bond. Therefore, for halogens

(Cl > Br > I), the bond-strength progresses from metal-Cl (strongest) to metal-I (weakest) following the EN trend: Cl (3.16) > Br (2.96) > I (2.66) on Pauling's scale.[72] In the chalcogen family we have S (2.58) \simeq Se (2.55) > Te (2.10), which explains the almost identical affect of S and Se on the formation energy and the weakest stability for the Te-based systems. Conversely, both metal sites in MMCHs are electron donors. With a lower EN they can transfer their valence electrons more easily to the electron acceptor sites for creating stronger chemical metal-Ch and metal-X bonds in the process. An inverse relation between the EN of the metal sites and stability ensues, which we see reflected in, e.g., the M(II)-site elements In (1.78) < Bi (1.90) < Sb (2.05). Also, Pb-based MMCHs are more stable than their Sn-based analogues in line with the respective EN values (1.80 and 1.96).

Figure 2 shows that the X-site element has the largest effect on the MMCH formation energy, followed by the Ch-, M(III)-, then M(II)-sites. The difference in impact can also be rationalized by the differences in the respective EN values. For the dominant X-site they span the largest range (0.50), followed by the Ch-, M(III)-, then M(II)-sites (0.48, 0.27, and 0.16, respectively).

Secondly, we found that the fundamental band gap (same applies to the lowest direct and optical band gaps, see Section III B) are mainly influenced by the Ch-site and both metal sites. Furthermore, we showed that the halogens have the smallest effect on the fundamental band gap (see Figure 3a), a trend opposite to the formation energy. These trends can be traced back to the orbital character of the halogens, chalcogens, and both ns^2 lone pair metals. Halogen p orbitals are generally more localized than those of the chalcogens due to their higher EN and smaller atomic size.[72] This increased localization leads to a weaker orbital overlap and thus hybridization with the ns^2 lone pair orbitals of the metal sites.[73] In contrast, chalcogen p orbitals are more diffused thus increasing the orbital overlap and the hybridization with the ns^2 lone pair orbitals of the metal sites, and subsequently also the impact on the valence band maximum (VBM). The chalcogens therefore have a larger effect on the fundamental band gap than the halogens. Conversely, both M(II) and M(III) cations have a similar orbital character ($5s^2$ lone pair and $5p$ empty orbitals for Sn and Sb, as well as $6s^2$ lone pair and $6p$ empty orbitals for Pb and Bi) except for In (no lone pair)) and therefore their contribution to the fundamental band gap is expected to be similar.

The effects of the orbital analysis are reflected in the DOS near the VBM and the conduction band minimum (CBM). This is illustrated in Figure 6 for lead-based and lead-free

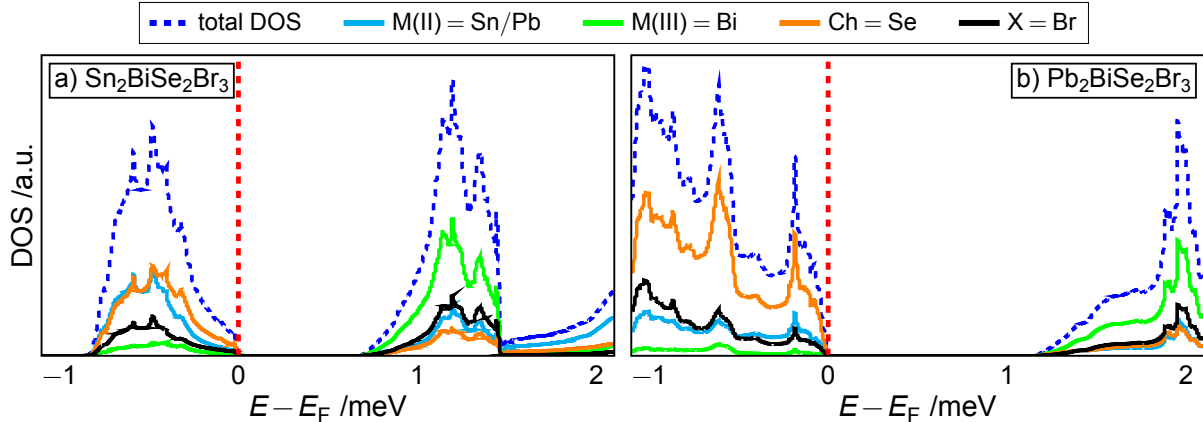


Figure 6. Density of state for a) $\text{Sn}_2\text{BiSe}_2\text{Br}_3$ and b) $\text{Pb}_2\text{BiSe}_2\text{Br}_3$ at $Cmcm$ phase.

$\text{M(II)BiSe}_2\text{Br}_3$ compounds as examples. Additionally, Figure SM 18 shows the corresponding $Cmc2_1$ and $P2_1/c$ phases. The chalcogens (orange) provide the largest contribution to the total DOS (dashed blue) near the VBM, primarily through the closed Se $4p^6$ shell. The contribution of the M(II) metals (cyan) is caused by the strong ns^2 anti-bonding character, whose important effect on the electronic structure of halide perovskites have been reported previously.[74–76] In contrast, the M(III) metals (light green) provide the largest contribution to the total DOS near the CBM via their empty p orbitals. Notably, the halogens (black) contribute significantly to the valence band (although less than the chalcogens, primarily due to the higher EN of halogens) but only minimally to the CBM. In summary, the hole states (near the VBM) are primarily determined by the chalcogens and the M(II) metals, while the free electron states (near the CBM) are mainly influenced by the M(III) metals. The fundamental band gap in MMCHs is therefore strongly affected by the chalcogen- ns^2 lone pair bonds. The corresponding band structures are shown in Figure SM 19. This character is different to halide perovskites for which the monovalent metal (or organic) cation provide negligible contribution to both band edges. Their impact on the electronic structure is indirect (via the crystal structure). In this regard, mixed-metal chalcohalides offer more options for tailoring the electronic structure than halide perovskites.

The design rules we derive from the SHAP analysis (see Figure 3b) for the band gap are generally similar to the ones for the formation energy, i.e., the larger EN for the nonmetals and the smaller EN for the metals, the higher the stability and the larger the band gap. For the M(III) we observe an exception. The reverse EN trend $\text{In} > \text{Bi} > \text{Sb}$ for the formation

energy does not hold for the band gap ($\text{In} > \text{Sb} > \text{Bi}$). The absence of the ns^2 lone pair in In^{3+} gives rise to a larger band gap in In-based MMCHs, breaking the trend. Conversely, the strong spin-orbital coupling induced by Bi significantly reduces the band gaps of Bi-based compounds to lower than those of the isostructural Sb-based analogs, a trend opposite to that observed for Pb vs. Sn.

The observation that the fundamental band gap in MMCH compounds decreases from Cl via Br to I and from Pb to Sn is also found in ABX_3 perovskites.[77–81] Furthermore, Nie *et al.* and Islam *et al.* report a decrease of the optical band gap from $\text{Sn}_2\text{SbS}_2\text{I}_3$ (1.41 eV) to $\text{Sn}_2\text{BiS}_2\text{I}_3$ (1.22 eV)[16, 25] in agreement with our observed design rule for the M(III)-site ($\text{Sb} > \text{Bi}$). This agrees well with our calculated values, 1.547 and 1.390 eV, see Table SM I. Moreover, we observe similar band gap trends in chalcogenides and sesquioxides for the M(III)-site. Huerta-Flores *et al.* measured a band gap decrease from In_2S_3 to Sb_2S_3 to Bi_2S_3 ($2.10 > 1.80 > 1.70$ eV) [82] that is found also in DFT calculations by Matsumoto *et al.* for oxides ($\text{As}_2\text{O}_3 > \text{Sb}_2\text{O}_3 > \text{Bi}_2\text{O}_3$).[83] These comparisons illustrate the consistency of our band gap design rules with the available literature and across different materials spaces.

Thirdly, our results show that the conduction bands in MMCH materials are more curved than the valence bands meaning smaller effective electron masses than hole masses, especially in the $Cmcm$ and $Cmc2_1$ phases. The curvature at the VBM is almost the same regardless of the phase. However, small changes in the chemical nature of MMCH compounds can shift their band structure and curvature, leading to inconsistent trends in effective masses across all three phases. Despite this, we found consistent patterns for the impact of halogens and metals at the M(II)-site on electron and hole effective masses. Specifically, the effective masses decrease in the order of $\text{Cl} > \text{Br} > \text{I}$ for halogens, and $\text{Pb} > \text{Sn}$ for metals. These trends match well with previous studies for ABX_3 [84–86] and two-dimensional halide perovskites.[87] Ashari-Astani *et al.* used tight binding and $\mathbf{k} \cdot \mathbf{p}$ theory to establish a strong linear relationship between the effective electron and hole masses and the fundamental band gap in lead-free and lead-based ABX_3 perovskites. They attributed this correlation, especially for holes, to the orbital overlap between halogens on the X-site and metal atoms on the B-site. We observe a similar correlation in MMCHs. Regardless of the phase, effective masses decrease in the order of $\text{Cl} > \text{Br} > \text{I}$ for the X-site, and $\text{Pb} > \text{Sn}$ for the M(II)-site, matching the fundamental band gap trends. The correlation between effective masses and band gap suggests a significant orbital contribution from the X- ns^2 metals bond, consistent

with Ashari-Astani *et al.*’s explanation for ABX_3 perovskites. However, we find no consistent correlations for the Ch- and M(III)-sites, which we attribute to the different chemical environments in the different phases. The increasing number of M(III)-Ch bonds per stoichiometric unit (one in $Cmc2_1$, two in $Cmcm$ and three in $P2_1/c$) gives rise to different coordination polyhedra and therefore a different environment around the M(III)-Ch bonds. Due to this difference in local environments, the effective mass trends differ across the three phases.

The fact that our purely data-driven model qualitatively agrees with the “chemical intuition” of a human scientist (e.g. based on the well-established EN or orbital character) is reassuring and illustrates that machine learning can find chemical trends without needing the auxiliary information of element specific attributes. While site-specific dependencies (e.g., Cl > Br > I for stability and band gap) and their rationalization in terms of chemical descriptors like EN could have easily been deduced by human scientists, the quaternary nature of the MMCH materials space makes the deduction of chemical trends more challenging. Our data-driven models revealed the chemical trends, established their relative importance (e.g. X- and Ch-sites dominate over the metal sites for the formation energy) and enables the formulation of a correlation between different material parameters. This allows us to deepen our MMCH material spaces knowledge.

Finally, we can now use the atom site importance and design rules we have derived for materials design recommendations. Figure 7 summaries the atom site importance’s of the formation energies, fundamental band gaps, as well as of effective electron and hole masses for $Cmcm$. Also, see Figures SM 20 ($Cmc2_1$) and SM 21 ($P2_1/c$) for the other two phases.

We have demonstrated that the two electron acceptor sites (Ch and X) affect the materials properties more than the two electron donor sites (M(II) and M(III)). Future MMCH design studies can set the basic material properties with the two acceptor sites and finetune them for to desired applications with appropriate choices for the two donor sites.

Furthermore it is remarkable that the elements impact across the atomic sites is fairly consistent across all material parameters. While a correlation between band gaps and the effective masses of electrons and holes might be expected, it is rather surprising, that this relationship also extends to structural stability. This trend is particularly evident for choosing elements within the M(II)- and X-sites, see Table I. In contrast, the design rules vary to some extent at the M(III)- and Ch-sites (see Table I), leading to a more pronounced trade-off

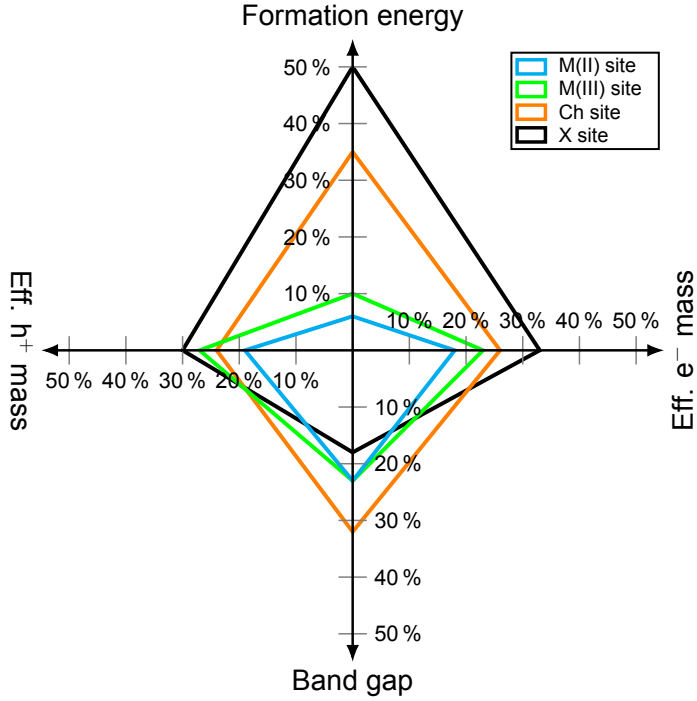


Figure 7. Summary of atom site importance on the formation energy, band gap, as well as the effective masses of electrons and holes in *Cmcm*.

between stability and electronic properties. For example, Sb and Se reduce the stability, but $M(II)_2SbSe_2X_3$ -based material exhibit preferable band gaps for photovoltaic applications with suitable electron effective masses, yet high hole masses. In contrast, swapping Sb for Bi increases the stability or Se for Te decreases it, but both substitutions lower the electron and hole masses and reduce the band gaps.

Overall, this allows adjustments toward either more stable materials with wider band gaps and heavier electrons and holes or less stable materials with narrower band gaps and lighter charge electrons and holes. Specifically, $Pb_2M(III)Ch_2Cl_3$ -based materials tend to be more stable with wider band gaps, whereas $Sn_2M(III)Ch_2I_3$ -based compounds shift to the opposite. In this context, $Pb_2SbSe_2Cl_3$ and $Sn_2BiS_2I_3$ stand out, combining relatively low charge carrier masses with band gaps of approximately 1.4 eV and 1.0 eV, respectively, making them promising candidates for further experimental and theoretical investigation.

Table I: Summary of the elements' impact on the formation energy, band gap as well as effective electron and hole masses within the atom sites. Color code indicates the relative importance of the atom site. green: largest impact; olive: 2nd largest impact; yellow: 2nd smallest impact; orange: smallest impact. Deviating trends within the space groups (for the effective electron and hole masses) are indicated by 1) *Cmcm*, 2) *Cmc2*₁ and 3) *P2*₁/*c*, otherwise the listed element trends are identical in all three space groups.

	M(II)-site	M(III)-site	Ch-site	X-site
Formation energy	Pb > Sn	In > Bi > Sb	S \simeq Se > Te	Cl > Br > I
Band gap	Pb > Sn	In > Sb > Bi	S > Se > Te	Cl > Br > I
		1) In > Bi \simeq Sb	1) S > Se > Te	
eff. electron mass	Pb > Sn	2) In > Bi > Sb	2) Te > Se > S	Cl > Br > I
		3) Bi > Sb > In	3) S > Se > Te	
		1) In > Bi \simeq Sb	1) S \simeq Se > Te	
eff. hole mass	Pb > Sn	2) Sb > Bi > In	2) S > Se \simeq Te	Cl > Br > I
		3) Sb > In \simeq Bi	3) Se > S > Te	

V. CONCLUSION

In conclusion, this study aimed to investigate the chemical trends governing material properties in perovskite-inspired quaternary mixed-metal chalcohalides. By analyzing thermodynamic stability, band gaps, and effective electron and hole masses through a combination of DFT, RF, and SHAP, we found that the electron acceptor sites (Ch and X) play a primary role in determining MMCH characteristics, while the electron donor sites (M(II) and M(III)) provide opportunities for fine-tuning material properties for specific applications. The choice of M(III) and Ch site occupants often introduces a trade-off when optimizing stability and electronic properties, whereas M(II) and halogen sites tend to affect both properties in the same way. Our findings across three crystal structures (*Cmcm*,

Cmc2₁, *P2₁/c*) further highlight the importance of structural diversity, as *P2₁/c* is the equilibrium phase at low temperatures with larger and mostly indirect fundamental band gaps, whereas *Cmcm* and *Cmc2₁* exhibit smaller and more direct band gaps. While effective hole masses are similar in all three phases, electron effective masses are smaller in *Cmcm* and *Cmc2₁* compared to *P2₁/c*. These results deepen our understanding of the relationship between composition, structure, and material properties in MMCHs, opening new avenues for optimizing optoelectronic applications, such as indoor and outdoor photovoltaics. Future research could build on these identified chemical rules to explore design strategies for enhancing MMCH performance.

ACKNOWLEDGMENTS

The authors thank Milica Todorović, Armi Tiihonen and Jarno A. Laakso for fruitful discussions. This study was supported by the Academy of Finland through Project No. 334532, the European Union’s Horizon 2020 research and innovation programme under the Marie Skłodowska-Curie grant agreement No. 101152684, the National Natural Science Foundation of China (Grant No. 22473088) and the Natural Science Foundation of Shaanxi Province of China (Grant No. 2023-YBGY-447). PH, JL and PR further acknowledge CSC-IT Center for Science, Finland, the Aalto Science-IT project, Xi'an Jiaotong University's HPC platform and the Computing Center in Xi'an of China for generous computational resources.

[1] S.-P. Feng, Y. Cheng, H.-L. Yip, Y. Zhong, P. W. K. Fong, G. Li, A. Ng, C. Chen, L. A. Castriotta, F. Matteocci, L. Vesce, D. Saranin, A. D. Carlo, P. Wang, J. Wei Ho, Y. Hou, F. Lin, A. G. Aberle, Z. Song, Y. Yan, X. Chen, Y. M. Yang, A. A. Syed, I. Ahmad, T. Leung, Y. Wang, J. Lin, A. M. C. Ng, Y. Li, F. Ebadi, W. Tress, G. Richardson, C. Ge, H. Hu, M. Karimipour, F. Baumann, K. Tabah, C. Pereyra, S. R. Raga, H. Xie, M. Lira-Cantu, M. V. Khenkin, I. Visoly-Fisher, E. A. Katz, Y. Vaynzof, R. Vidal, G. Yu, H. Lin, S. Weng, S. Wang, and A. B. Djurišić, Roadmap on commercialization of metal halide perovskite photovoltaics, *Journal of Physics: Materials* **6**, 032501 (2023).

- [2] W. Zhang, G. E. Eperon, and H. J. Snaith, Metal halide perovskites for energy applications, *Nature Energy* **1**, 16048 (2016).
- [3] National Renewable Energy Laboratory. *Best Research-Cell Efficiencies Chart*. <https://www.nrel.gov/pv/cell-efficiency.html> (accessed November 20, 2025).
- [4] J. Seo, J. H. Noh, and S. I. Seok, Rational Strategies for Efficient Perovskite Solar Cells, *Accounts of Chemical Research* **49**, 562 (2016).
- [5] R. Nie, K. S. Lee, M. Hu, M. J. Paik, and S. I. Seok, Heteroleptic Tin-Antimony Sulfoiodide for Stable and Lead-free Solar Cells, *Matter* **3**, 1701 (2020).
- [6] K. J. Savill, A. M. Ulatowski, and L. M. Herz, Optoelectronic Properties of Tin–Lead Halide Perovskites, *ACS Energy Letters* **6**, 2413 (2021).
- [7] Y.-T. Huang, S. R. Kavanagh, D. O. Scanlon, A. Walsh, and R. L. Z. Hoye, Perovskite-Inspired Materials for Photovoltaics and beyond— from Design to Devices, *Nanotechnology* **32**, 132004 (2021).
- [8] Y.-T. Huang, S. R. Kavanagh, D. O. Scanlon, A. Walsh, and R. L. Z. Hoye, Corrigendum: Perovskite-inspired Materials for Photovoltaics and beyond— from Design to Devices (2021 Nanotechnology 32 132004), *Nanotechnology* **32**, 379501 (2021).
- [9] A. M. Ganose, C. N. Savory, and D. O. Scanlon, Beyond Methylammonium Lead Iodide: Prospects for the Emergent Field of $Ns\text{\textsuperscript}2$ Containing Solar Absorbers, *Chemical Communications* **53**, 20 (2017).
- [10] J. Cao and F. Yan, Recent Progress in Tin-Based Perovskite Solar Cells, *Energy & Environmental Science* **14**, 1286 (2021).
- [11] S. H. Im, H.-j. Kim, S. W. Kim, S.-W. Kim, and S. I. Seok, All Solid State Multiply Layered PbS Colloidal Quantum-Dot-Sensitized Photovoltaic Cells, *Energy & Environmental Science* **4**, 4181 (2011).
- [12] Y.-L. Lee and Y.-S. Lo, Highly Efficient Quantum-Dot-Sensitized Solar Cell Based on Co-Sensitization of CdS/CdSe, *Advanced Functional Materials* **19**, 604 (2009).
- [13] Y. C. Choi, D. U. Lee, J. H. Noh, E. K. Kim, and S. I. Seok, Highly Improved Sb $\text{\textsubscript}2$ S $\text{\textsubscript}3$ Sensitized-Inorganic-Organic Heterojunction Solar Cells and Quantification of Traps by Deep-Level Transient Spectroscopy, *Advanced Functional Materials* **24**, 3587 (2014).

- [14] S. R. Kavanagh, A. Walsh, and D. O. Scanlon, Rapid Recombination by Cadmium Vacancies in CdTe, *ACS Energy Letters* , 1392 (2021).
- [15] V. Yadav, S. Kashyap, R. Pandey, and J. Madan, Impact of Doping Variation on the Performance of Sb_2S_3 based Solar Cell using Device Simulations, in *2023 IEEE Devices for Integrated Circuit (DevIC)* (IEEE, Kalyani, India, 2023) pp. 52–55.
- [16] R. Nie, R. R. Sumukam, S. H. Reddy, M. Banavoth, and S. I. Seok, Lead-Free Perovskite Solar Cells Enabled by Hetero-Valent Substitutes, *Energy & Environmental Science* **13**, 2363 (2020).
- [17] S. R. Kavanagh, C. N. Savory, D. O. Scanlon, and A. Walsh, Hidden Spontaneous Polarisation in the Chalcohalide Photovoltaic Absorber $\text{Sn}_2\text{SbS}_2\text{I}_3$, *Materials Horizons* **8**, 2709 (2021).
- [18] K. V. Sopiha, C. Comparotto, J. A. Márquez, and J. J. S. Scragg, Chalcogenide Perovskites: Tantalizing Prospects, *Challenging Materials*, *Advanced Optical Materials* **10**, 2101704 (2022).
- [19] A. Kojima, K. Teshima, Y. Shirai, and T. Miyasaka, Organometal Halide Perovskites as Visible-Light Sensitizers for Photovoltaic Cells, *Journal of the American Chemical Society* **131**, 6050 (2009).
- [20] P. Henkel, J. Li, G. K. Grandhi, P. Vivo, and P. Rinke, Screening Mixed-Metal $\text{Sn}_2\text{M(III)}\text{Ch}_2\text{X}_3$ Chalcohalides for Photovoltaic Applications, *Chemistry of Materials* **35**, 7761 (2023).
- [21] J. Olivier-Fourcade, J. C. Jumas, M. Maurin, and E. Philippot, Mise en Évidence d'un Nouveau Sulfoiodure d'Étain et d'Antimoine $\text{Sn}_2\text{SbS}_2\text{I}_3$: Étude Structurale, *Zeitschrift für anorganische und allgemeine Chemie* **468**, 91 (1980).
- [22] A. Nicolson, J. Breternitz, S. R. Kavanagh, Y. Tomm, K. Morita, A. G. Squires, M. Tovar, A. Walsh, S. Schorr, and D. O. Scanlon, Interplay of Static and Dynamic Disorder in the Mixed-Metal Chalcohalide $\text{Sn}_2\text{SbS}_2\text{I}_3$, *Journal of the American Chemical Society* **145**, 12509 (2023).
- [23] A. N. Roth, A. P. Porter, S. Horger, K. Ochoa-Romero, G. Guirado, A. J. Rossini, and J. Vela, Lead-Free Semiconductors: Phase-Evolution and Superior Stability of Multinary Tin Chalcohalides, *Chemistry of Materials* **36**, 4542 (2024).
- [24] A. Ibanez, J.-C. Jumas, J. Olivier-Fourcade, and E. Philippot, Mise en évidence d'un désordre statistique dans les structures chalcogénoiodures d'étain et d'antimoine, *Journal of Solid State Chemistry* **55**, 83 (1984).

[25] S. M. Islam, C. D. Malliakas, D. Sarma, D. C. Maloney, C. C. Stoumpos, O. Y. Kontsevoi, A. J. Freeman, and M. G. Kanatzidis, Direct Gap Semiconductors $\text{Pb}_2\text{BiS}_2\text{I}_3$, $\text{Sn}_2\text{BiS}_2\text{I}_3$, and Sn_2BiSI_5 , *Chemistry of Materials* **28**, 7332 (2016).

[26] V. Dolgikh, New Chalkogen-Halogenides of the Type $\text{M}_2\text{SbS}_2\text{I}_3$, *Izv. Akad. Nauk SSSR, Neorg. Mater.* **21**, 1211 (1985).

[27] C. Doussier, Y. Moëlo, P. Léone, A. Meerschaut, and M. Evain, Crystal Structure of $\text{Pb}_2\text{Sb}_2\text{I}_3$, and Re-Examination of the Crystal Chemistry within the Group of (Pb/Sn/Sb) Chalcogeno-Iodides, *Solid State Sciences* **9**, 792 (2007).

[28] A. N. Roth, J. Opare-Addo, E. Gi, S. Mena, G. Guirado, R. D. Schaller, E. A. Smith, and J. Vela, Solution-Phase Synthesis and Photoluminescence of Quaternary Chalcohalide Semiconductors, *Chemistry of Materials* **35**, 2165 (2023).

[29] See Supplemental Material at <http://link.aps.org/supplemental/10.1103/qjwt-29w9> for I) RF regression model performance per phase for the studied material properties (formation energies, fundamental band gaps, and effective electron and hole masses), II) tabulated computed values for formation energies, fundamental band gaps, minimal direct band gaps, optical band gaps, as well as effective electron and hole masses for all MMCH materials in all three phases, III) RF regression model performance and results for minimum direct band gaps and optical band gaps in all three phases, IV) DOS of lead-free and lead-based $\text{M(II)}_2\text{BiSe}_2\text{Br}_3$ compounds in $\text{Cmc}2_1$ and $\text{P}2_1/c$ phase, V) Band structures of lead-free and lead-based $\text{M(II)}_2\text{BiSe}_2\text{Br}_3$ compounds in all three phases and VI) Comparison of MMCHs material properties in $\text{Cmc}2_1$ and $\text{P}2_1/c$ phases, which includes Ref. [88].

[30] A. Jain, S. P. Ong, G. Hautier, W. Chen, W. D. Richards, S. Dacek, S. Cholia, D. Gunter, D. Skinner, G. Ceder, and K. A. Persson, Commentary: The Materials Project: A Materials Genome Approach to Accelerating Materials Innovation, *APL Materials* **1**, 011002 (2013).

[31] K. Momma and F. Izumi, \emph{VESTA} : A Three-Dimensional Visualization System for Electronic and Structural Analysis, *Journal of Applied Crystallography* **41**, 653 (2008).

[32] V. Blum, R. Gehrke, F. Hanke, P. Havu, V. Havu, X. Ren, K. Reuter, and M. Scheffler, Ab Initio Molecular Simulations with Numeric Atom-Centered Orbitals, *Computer Physics Communications* **180**, 2175 (2009).

[33] V. Havu, V. Blum, P. Havu, and M. Scheffler, Efficient Integration for All-Electron Electronic Structure Calculation Using Numeric Basis Functions, *Journal of Computational Physics* **228**,

8367 (2009).

- [34] X. Ren, P. Rinke, V. Blum, J. Wieferink, A. Tkatchenko, A. Sanfilippo, K. Reuter, and M. Scheffler, Resolution-of-Identity Approach to Hartree–Fock, Hybrid Density Functionals, RPA, MP2 and GW with Numeric Atom-Centered Orbital Basis Functions, *New Journal of Physics* **14**, 053020 (2012).
- [35] S. V. Levchenko, X. Ren, J. Wieferink, R. Johanni, P. Rinke, V. Blum, and M. Scheffler, Hybrid Functionals for Large Periodic Systems in an All-Electron, Numeric Atom-Centered Basis Framework, *Computer Physics Communications* **192**, 60 (2015).
- [36] V. W.-z. Yu, F. Corsetti, A. García, W. P. Huhn, M. Jacquelin, W. Jia, B. Lange, L. Lin, J. Lu, W. Mi, A. Seifitokaldani, Á. Vázquez-Mayagoitia, C. Yang, H. Yang, and V. Blum, ELSI: A Unified Software Interface for Kohn–Sham Electronic Structure Solvers, *Computer Physics Communications* **222**, 267 (2018).
- [37] A. C. Ihrig, J. Wieferink, I. Y. Zhang, M. Ropo, X. Ren, P. Rinke, M. Scheffler, and V. Blum, Accurate Localized Resolution of Identity Approach for Linear-Scaling Hybrid Density Functionals and for Many-Body Perturbation Theory, *New Journal of Physics* **17**, 093020 (2015).
- [38] J. P. Perdew, A. Ruzsinszky, G. I. Csonka, O. A. Vydrov, G. E. Scuseria, L. A. Constantin, X. Zhou, and K. Burke, Restoring the Density-Gradient Expansion for Exchange in Solids and Surfaces, *Physical Review Letters* **100**, 136406 (2008).
- [39] J. P. Perdew, A. Ruzsinszky, G. I. Csonka, O. A. Vydrov, G. E. Scuseria, L. A. Constantin, X. Zhou, and K. Burke, Erratum: Restoring the Density-Gradient Expansion for Exchange in Solids and Surfaces [Phys. Rev. Lett. **100**, 136406 (2008)], *Physical Review Letters* **102**, 039902 (2009).
- [40] R. X. Yang, J. M. Skelton, E. L. da Silva, J. M. Frost, and A. Walsh, Spontaneous Octahedral Tilting in the Cubic Inorganic Cesium Halide Perovskites CsSnX_3 and CsPbX_3 ($\text{X} = \text{F}, \text{Cl}, \text{Br}, \text{I}$), *The Journal of Physical Chemistry Letters* **8**, 4720 (2017).
- [41] M. Bokdam, J. Lahnsteiner, B. Ramberger, T. Schäfer, and G. Kresse, Assessing Density Functionals Using Many Body Theory for Hybrid Perovskites, *Physical Review Letters* **119**, 145501 (2017).
- [42] J. Laakso, M. Todorović, J. Li, G.-X. Zhang, and P. Rinke, Compositional engineering of perovskites with machine learning, *Physical Review Materials* **6**, 113801 (2022).

[43] F. Pan, J. Zhai, J. Chen, L. Yang, H. Dong, F. Yuan, Z. Jiang, W. Ren, Z.-G. Ye, G.-X. Zhang, and J. Li, Mixed-Halide Perovskite Alloys $\text{CsPb}(\text{I}_{1-x}\text{Br}_x)_3$ and $\text{CsPb}(\text{Br}_{1-x}\text{Cl}_x)_3$: New Insight of Configurational Entropy Effect from First-Principles and Phase Diagrams, *Chemistry of Materials* **36**, 3957 (2024).

[44] J. Li, F. Pan, G.-X. Zhang, Z. Liu, H. Dong, D. Wang, Z. Jiang, W. Ren, Z.-G. Ye, M. Todorović, and P. Rinke, Structural Disorder by Octahedral Tilting in Inorganic Halide Perovskites: New Insight with Bayesian Optimization, *Small Structures* , 2400268 (2024).

[45] F. Knuth, C. Carbogno, V. Atalla, V. Blum, and M. Scheffler, All-Electron Formalism for Total Energy Strain Derivatives and Stress Tensor Components for Numeric Atom-Centered Orbitals, *Computer Physics Communications* **190**, 33 (2015).

[46] E. van Lenthe, E. J. Baerends, and J. G. Snijders, Relativistic Regular Two-component Hamiltonians, *The Journal of Chemical Physics* **99**, 4597 (1993).

[47] J. Heyd, G. E. Scuseria, and M. Ernzerhof, Hybrid Functionals Based on a Screened Coulomb Potential, *The Journal of Chemical Physics* **118**, 8207 (2003).

[48] J. Heyd, G. E. Scuseria, and M. Ernzerhof, Erratum: “Hybrid Functionals Based on a Screened Coulomb Potential” [J. Chem. Phys. 118, 8207 (2003)], *The Journal of Chemical Physics* **124**, 219906 (2006).

[49] A. V. Krukau, O. A. Vydrov, A. F. Izmaylov, and G. E. Scuseria, Influence of the Exchange Screening Parameter on the Performance of Screened Hybrid Functionals, *The Journal of Chemical Physics* **125**, 224106 (2006).

[50] W. P. Huhn and V. Blum, One-Hundred-Three Compound Band-Structure Benchmark of Post-Self-Consistent Spin-Orbit Coupling Treatments in Density Functional Theory, *Physical Review Materials* **1**, 033803 (2017).

[51] L. D. Whalley, Effmass: An effective mass package, *Journal of Open Source Software* **3**, 797 (2018).

[52] C. Ambrosch-Draxl and J. O. Sofo, Linear Optical Properties of Solids within the Full-Potential Linearized Augmented Planewave Method, *Computer Physics Communications* **175**, 1 (2006).

[53] C. G. Van de Walle and J. Neugebauer, Structure and Energetics of Nitride Surfaces under MOCVD Growth Conditions, *Journal of Crystal Growth* **248**, 8 (2003).

[54] L. Himanen, A. Geurts, A. S. Foster, and P. Rinke, Data-Driven Materials Science: Status, Challenges, and Perspectives, *Advanced Science* **6**, 1900808 (2019).

[55] P. Henkel, J. Li, and P. Rinke, NOMAD dataset: Lead-free $\text{Sn}_2\text{M(II)}\text{Ch}_2\text{X}_3$ materials (2023).

[56] P. Henkel, J. Li, and P. Rinke, NOMAD dataset: Lead-based $\text{Pb}_2\text{M(II)}\text{Ch}_2\text{X}_3$ materials (2025).

[57] L. Breiman, Random forests, *Machine Learning* **45**, 5 (2001).

[58] G. James, D. Witten, T. Hastie, and R. Tibshirani, *An Introduction to Statistical Learning*, Springer Texts in Statistics, Vol. 103 (Springer New York, New York, NY, 2013).

[59] F. Pedregosa, G. Varoquaux, A. Gramfort, V. Michel, B. Thirion, O. Grisel, M. Blondel, P. Prettenhofer, R. Weiss, V. Dubourg, J. Vanderplas, A. Passos, D. Cournapeau, M. Brucher, M. Perrot, and E. Duchesnay, Scikit-learn: Machine learning in Python, *Journal of Machine Learning Research* **12**, 2825 (2011).

[60] Y. Huang, C. Yu, W. Chen, Y. Liu, C. Li, C. Niu, F. Wang, and Y. Jia, Band gap and band alignment prediction of nitride-based semiconductors using machine learning, *Journal of Materials Chemistry C* **7**, 3238 (2019).

[61] V. Gladkikh, D. Y. Kim, A. Hajibabaei, A. Jana, C. W. Myung, and K. S. Kim, Machine Learning for Predicting the Band Gaps of ABX_3 Perovskites from Elemental Properties, *The Journal of Physical Chemistry C* **124**, 8905 (2020).

[62] G. Pilania, A. Mannodi-Kanakkithodi, B. P. Uberuaga, R. Ramprasad, J. E. Gubernatis, and T. Lookman, Machine learning bandgaps of double perovskites, *Scientific Reports* **6**, 19375 (2016).

[63] T. A. R. Purcell, M. Scheffler, C. Carbogno, and L. M. Ghiringhelli, SISSO++: A C++ Implementation of the Sure-IndependenceScreening and Sparsifying Operator Approach, *Journal of Open Source Software* **7**, 3960 (2022).

[64] S. M. Lundberg and S.-I. Lee, A unified approach to interpreting model predictions, in *Advances in Neural Information Processing Systems*, Vol. 30, edited by I. Guyon, U. V. Luxburg, S. Bengio, H. Wallach, R. Fergus, S. Vishwanathan, and R. Garnett (Curran Associates, Inc., 2017).

[65] S. M. Lundberg, G. Erion, H. Chen, A. DeGrave, J. M. Prutkin, B. Nair, R. Katz, J. Himmelfarb, N. Bansal, and S.-I. Lee, From local explanations to global understanding with explainable AI for trees, *Nature Machine Intelligence* **2**, 56 (2020).

[66] S. M. Lundberg, G. G. Erion, and S.-I. Lee, Consistent Individualized Feature Attribution for Tree Ensembles (2018).

[67] S. M. Lundberg, SHAP.

[68] W. Kaiser, D. Ricciarelli, E. Mosconi, A. A. Alothman, F. Ambrosio, and F. De Angelis, Stability of Tin- versus Lead-Halide Perovskites: Ab Initio Molecular Dynamics Simulations of Perovskite/Water Interfaces, *The Journal of Physical Chemistry Letters* **13**, 2321 (2022).

[69] J. Pascual, G. Nasti, M. H. Aldamasy, J. A. Smith, M. Flatken, N. Phung, D. Di Girolamo, S.-H. Turren-Cruz, M. Li, A. Dallmann, R. Avolio, and A. Abate, Origin of Sn(II) oxidation in tin halide perovskites, *Materials Advances* **1**, 1066 (2020).

[70] A. F. Akbulatov, S. A. Tsarev, M. Elshobaki, S. Y. Luchkin, I. S. Zhidkov, E. Z. Kurmaev, S. M. Aldoshin, K. J. Stevenson, and P. A. Troshin, Comparative Intrinsic Thermal and Photochemical Stability of Sn(II) Complex Halides as Next-Generation Materials for Lead-Free Perovskite Solar Cells, *The Journal of Physical Chemistry C* **123**, 26862 (2019).

[71] T. Leijtens, R. Prasanna, A. Gold-Parker, M. F. Toney, and M. D. McGehee, Mechanism of Tin Oxidation and Stabilization by Lead Substitution in Tin Halide Perovskites, *ACS Energy Letters* **2**, 2159 (2017).

[72] J. R. Rumble, T. J. Brunno, and M. J. Doa, eds., *CRC Handbook of Chemistry and Physics: A Ready-Reference Book of Chemical and Physical Data*, 104th ed., CRC Handbook of Chemistry and Physics / Chemical Rubber Company No. 104th edition (2023/2024) (CRC Press, Boca Raton London New York, 2023).

[73] H. Shi, D. Han, S. Chen, and M.-H. Du, Impact of metal ns^2 lone pair on luminescence quantum efficiency in low-dimensional halide perovskites, *Phys. Rev. Materials* **3**, 034604.

[74] J. M. Frost and A. Walsh, What Is Moving in Hybrid Halide Perovskite Solar Cells?, *Accounts of Chemical Research* **49**, 528 (2016).

[75] F. Brivio, A. B. Walker, and A. Walsh, Structural and electronic properties of hybrid perovskites for high-efficiency thin-film photovoltaics from first-principles, *APL Materials* **1**, 042111 (2013).

[76] A. Walsh, D. J. Payne, R. G. Egddell, and G. W. Watson, Stereochemistry of post-transition metal oxides: Revision of the classical lone pair model, *Chemical Society Reviews* **40**, 4455 (2011).

[77] F. Hao, C. C. Stoumpos, R. P. H. Chang, and M. G. Kanatzidis, Anomalous Band Gap Behavior in Mixed Sn and Pb Perovskites Enables Broadening of Absorption Spectrum in Solar Cells, *Journal of the American Chemical Society* **136**, 8094 (2014).

[78] Z. Yang, A. Rajagopal, C.-C. Chueh, S. B. Jo, B. Liu, T. Zhao, and A. K.-Y. Jen, Stable Low-Bandgap Pb–Sn Binary Perovskites for Tandem Solar Cells, *Advanced Materials* **28**, 8990 (2016).

[79] J. Li, Q. Wang, and A. Abate, Perovskite solar cells, in *Nanomaterials for Solar Cell Applications* (Elsevier, 2019) pp. 417–446.

[80] R. Kour, S. Arya, S. Verma, J. Gupta, P. Bandhoria, V. Bharti, R. Datt, and V. Gupta, Potential Substitutes for Replacement of Lead in Perovskite Solar Cells: A Review, *Global Challenges* **3**, 1900050 (2019).

[81] Z. Yang, A. Rajagopal, S. B. Jo, C.-C. Chueh, S. Williams, C.-C. Huang, J. K. Katahara, H. W. Hillhouse, and A. K.-Y. Jen, Stabilized Wide Bandgap Perovskite Solar Cells by Tin Substitution, *Nano Letters* **16**, 7739 (2016).

[82] A. M. Huerta-Flores, N. A. García-Gómez, S. M. De La Parra, and E. M. Sánchez, Comparative study of Sb₂S₃, Bi₂S₃ and In₂S₃ thin film deposition on TiO₂ by successive ionic layer adsorption and reaction (SILAR) method, *Materials Science in Semiconductor Processing* **37**, 235 (2015).

[83] A. Matsumoto, Y. Koyama, A. Togo, M. Choi, and I. Tanaka, Electronic structures of dynamically stable As₂O₃, Sb₂O₃, and Bi₂O₃ crystal polymorphs, *Physical Review B* **83**, 214110 (2011).

[84] J. Feng and B. Xiao, Effective Masses and Electronic and Optical Properties of Nontoxic MASnX₃ (X = Cl, Br, and I) Perovskite Structures as Solar Cell Absorber: A Theoretical Study Using HSE06, *The Journal of Physical Chemistry C* **118**, 19655 (2014).

[85] Y. Chen, L. Xiao, L. Shi, and P. Qian, High-throughput screening of the transport behavior of tetragonal perovskites, *Physical Chemistry Chemical Physics* **26**, 9378 (2024).

[86] N. Ashari-Astani, S. Meloni, A. H. Salavati, G. Palermo, M. Grätzel, and U. Rothlisberger, Computational Characterization of the Dependence of Halide Perovskite Effective Masses on Chemical Composition and Structure, *The Journal of Physical Chemistry C* **121**, 23886 (2017).

[87] M. Dyksik, H. Duim, X. Zhu, Z. Yang, M. Gen, Y. Kohama, S. Adjokatse, D. K. Maude, M. A. Loi, D. A. Egger, M. Baranowski, and P. Plochocka, Broad Tunability of Carrier

Effective Masses in Two-Dimensional Halide Perovskites, ACS Energy Letters **5**, 3609 (2020).

[88] V. I. Starosta, J. Kroutil, and L. Beneš, Preparation and Fundamental Physical Properties of $\text{Sn}_2\text{SbS}_2\text{I}_3$ and $\text{Pb}_2\text{SbS}_2\text{I}_3$ Compounds, Crystal Research and Technology **25**, 1439 (1990).

Supplemental Material for “Design Rules for Optimizing Quaternary Mixed-Metal Chalcohalides”

Pascal Henkel

*Department of Applied Physics, Aalto University,
P.O.Box 11100, FI-00076 AALTO, Finland*

Jingrui Li

*State Key Laboratory for Manufacturing Systems
Engineering; Electronic Materials Research Laboratory,
Key Laboratory of the Ministry of Education,
School of Electronic Science and Engineering; International Joint
Laboratory for Micro/Nano Manufacturing and Measurement Technology,
Xi'an Jiaotong University, Xi'an 710049, China*

Patrick Rinke

Physics Department, Technical University of Munich, Garching, Germany

*Atomistic Modelling Center, Munich Data Science Institute,
Technical University of Munich, Garching, Germany*

Munich Center for Machine Learning (MCML) and

*Department of Applied Physics, Aalto University,
P.O.Box 11100, FI-00076 AALTO, Finland*

**SM1: DESCRIPTION OF THE STRUCTURAL FEATURES OF
 $M(II)_2M(III)Ch_2X_3$ MATERIALS IN $Cmcm$, $Cmc2_1$ AND $P2_1/c$ PHASES**

The MMCH $Cmcm$ phase is characterized by the presence of $M(II)Ch_3X_2$ pyramids, which are edge-linked to form periodically continuous 1D $[M(II)_2Ch_2X_2]_n$ double chains along the a axis, see main text Figure 1a. These chains are joined via $M(III)X$ units and form 2D $M(II)_2M(III)Ch_2X_3$ structures within the ac plane which are not linked along the b axis. The $Cmc2_1$ structure is related to the $Cmcm$ structure except that the $M(III)X$ units are linked exclusively to a single $[M(II)_2Ch_2X_2]_n$ chain (in contrast to $Cmcm$ in which they are linked to 2 chains), interrupting the connection along the a axis and preventing the formation of 2D $M(II)_2M(III)Ch_2X_3$ units, see main text Figure 1b. Similar to $Cmcm$, $M(II)_2M(III)Ch_2X_3$ units are not connected along the b axis in $Cmc2_1$. In the $Cmc2_1$ phase, the asymmetric positioning of $M(III)$ between the chains causes every second square pyramidal $M(II)Ch_2X_3$ polyhedron to transform into a $M(II)X_3$ tetrahedron thus forming a 1D $[M(II)_2Ch_2X]_n$ chain, while simultaneously forming another square pyramidal $M(III)ChX_4$ polyhedron via the attachment of $M(II)X_2$ unit. The $P2_1/c$ phase differs from the other two. The primary structural features in the $P2_1/c$ phase are the $M(II)_4Ch_4X_8$ units, which consist of four pyramids: $M(II)ChX_4$, $M(II)Ch_3X_2$, $M(II)Ch_3X_2$, and $M(II)ChX_4$. In these units, the two $M(II)Ch_3X_2$ pyramids share edges, while the $M(II)ChX_4$ and $M(II)Ch_3X_2$ pyramids share faces, see main text Figure 1c). The neighboring $M(II)_4Ch_4X_8$ units share corners (X) within the bc planes, and are linked via two $M(III)$ atoms along the c axis to form square pyramidal $M(III)Ch_3X_2$ polyhedrons. This finally results in a 2D $M(II)_4M(III)_2Ch_4X_6$ structure within the bc plane.

SM2: PERFORMANCE OF THE ESTABILISED RANDOM FOREST REGRESSION MODELS TO PREDICT FORMATION ENERGIES, FUNDAMENTAL BAND GAPS, AS WELL AS EFFECTIVE ELECTRON AND HOLE MASSES

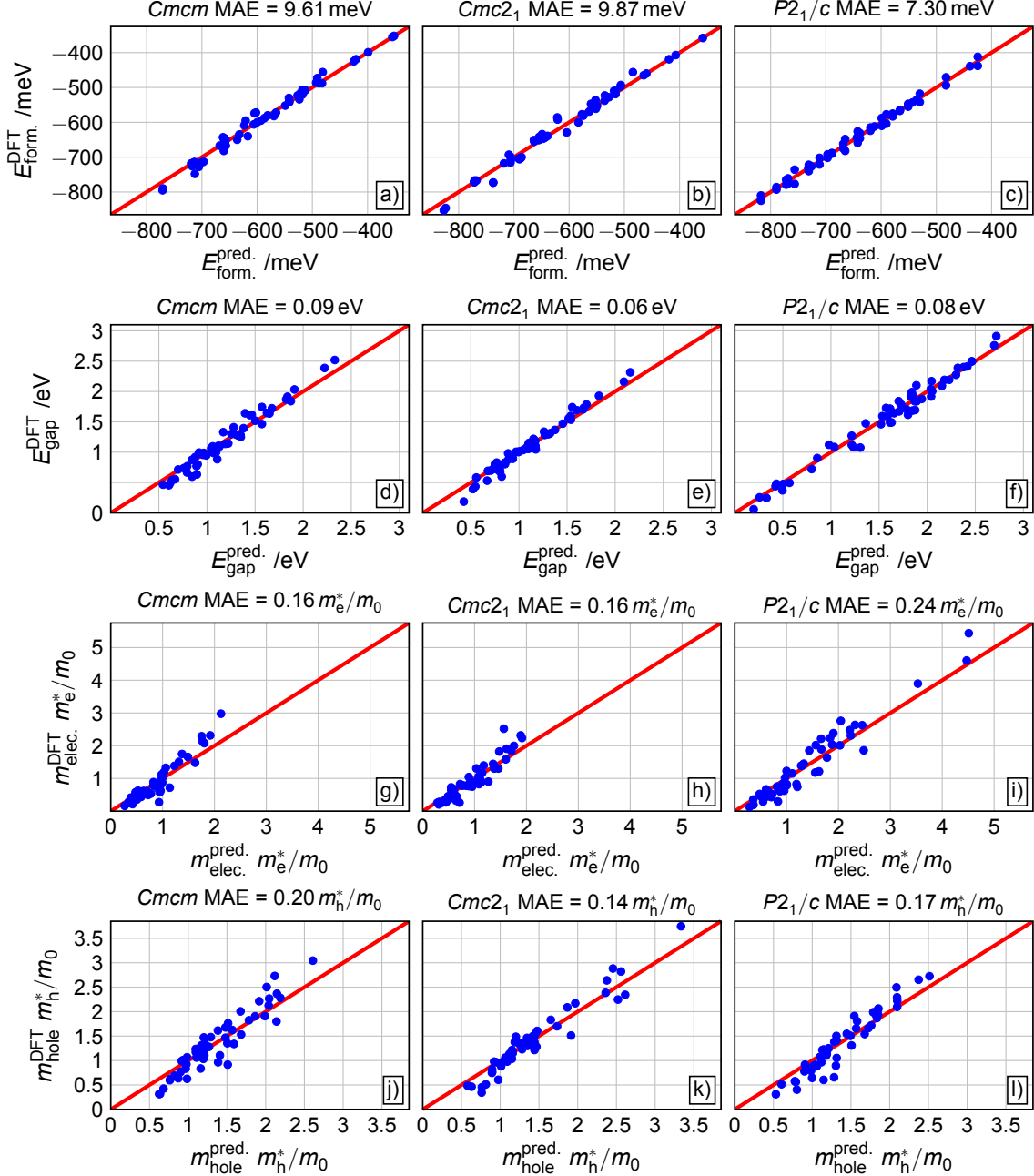


Figure 1. Machine learning (random forest regression) predicted a)-c) formation energies, d)-f) fundamental band gaps, f)-i) effective electron masses and j)-l) effective hole masses compared to their DFT optimized counterparts, within the a), f) g) & j) Cmcm, b), e), h) & k) Cmc₂1 as well as c), f), i) & l) P2₁/c phase.

SM3: PERFORMANCE OF THE ESTABLISHED RANDOM FOREST REGRESSION MODELS TO PREDICT LOWEST DIRECT BAND GAPS

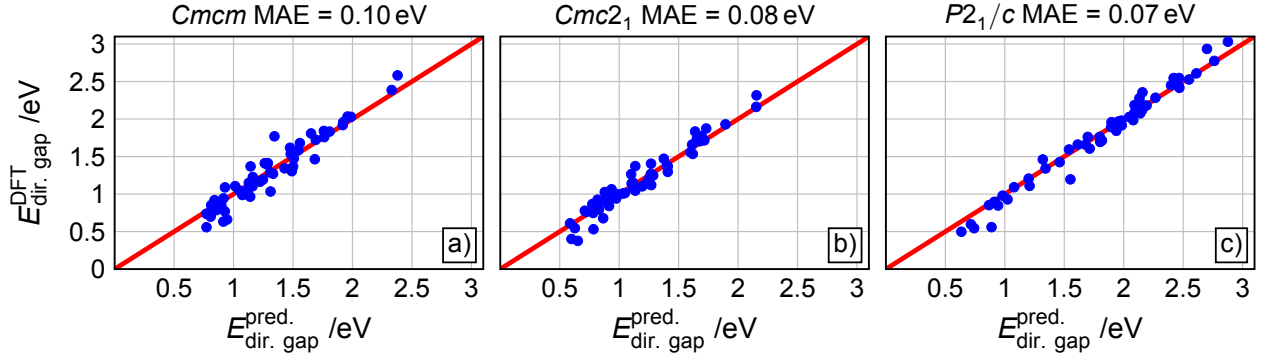


Figure 2. Machine learning (random forest regression) predicted lowest direct band gaps compared to DFT optimized lowest direct band gaps within a) $Cmcm$, b) $Cmc2_1$ as well as $P2_1/c$ phase. Corresponding interpretation of results are shown in SI Figures 8 for $Cmcm$, 9 for $Cmc2_1$ and 10 for $P2_1/c$.

SM4: PERFORMANCE OF THE ESTABLISHED RANDOM FOREST REGRESSION MODELS TO PREDICT OPTICAL BAND GAPS

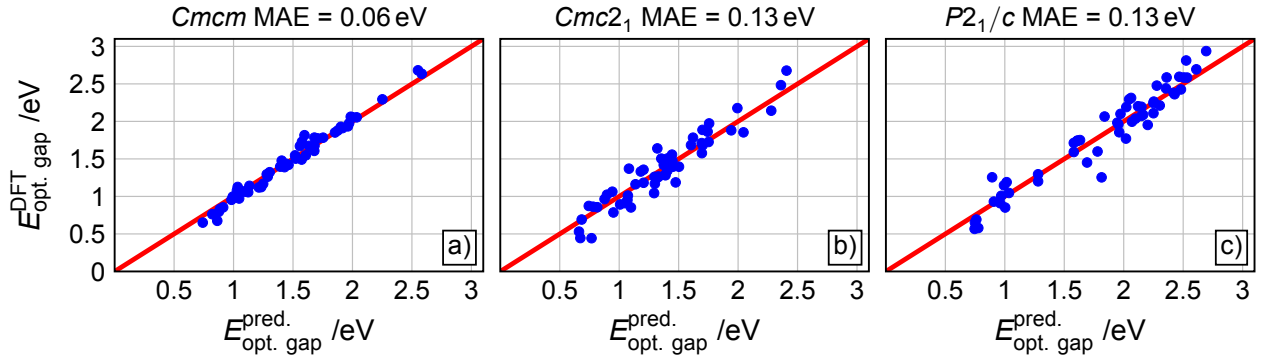


Figure 3. Machine learning (random forest regression) predicted optical band gaps compared to DFT optimized optical band gaps within a) $Cmcm$, b) $Cmc2_1$ as well as $P2_1/c$ phase. Corresponding interpretation of results are shown in SI Figures 11 for $Cmcm$, 12 for $Cmc2_1$ and 13 for $P2_1/c$.

SM5: LATTICE PARAMETERS, FORMATION ENERGIES, FUNDAMENTAL AND OPTICAL BAND GAPS, AS WELL AS EFFECTIVE ELECTRON AND HOLE MASSES FOR $M(II)_2M(III)Ch_2X_3$ MATERIALS

Table I. Density function theory calculated lattice parameters (a , b , c) formation energies E_{form} (related to the i -th elements) using PBEsol level of theory and fundamental band gaps E_g , and for indirect MMCH materials also the lowest indirect band gaps ($E_{g, \text{ind.}}$), optical band gaps as well as effective electron and hole masses using HSE06+SOC level of theory. -/- marks that either the material has no indirect/no band gap at all or that no experimental values are available.

System	Group	lat. parameters			E_{form} /eV Atom $^{-1}$	$E_{g, \text{dir.}}$ /eV	$E_{g, \text{ind.}}$ /eV	$E_{g, \text{opt.}}$ /eV	eff. masses	
		a /Å	b /Å	c /Å					m_e^*/m_0	m_h^*/m_0
$\text{Sn}_2\text{InS}_2\text{Cl}_3$	<i>Cmcm</i>	4.23	14.12	14.30	-726	1.31	1.25	1.49	0.62	1.91
	<i>Cmc21</i>	3.94	14.22	15.01	-772	1.83	1.69	1.89	1.99	1.38
	<i>P2₁/c</i>	6.27	16.19	7.88	-779	2.43	2.04	2.44	1.89	0.89
$\text{Sn}_2\text{InS}_2\text{Br}_3$	<i>Cmcm</i>	4.22	14.8	14.50	-650	1.62	-/-	1.98	0.87	1.35
	<i>Cmc21</i>	4.11	15.16	15.53	-693	1.74	-/-	1.78	1.82	2.09
	<i>P2₁/c</i>	6.36	16.55	8.07	-690	1.99	1.62	2.00	0.83	1.51
$\text{Sn}_2\text{InS}_2\text{I}_3$	<i>Cmcm</i>	4.37	15.68	14.83	-520	1.40	-/-	1.93	2.29	2.01
	<i>Cmc21</i>	4.06	14.13	19.25	-519	1.12	0.60	1.19	0.67	2.17
	<i>P2₁/c</i>	7.66	16.56	8.41	-565	2.28	2.10	2.31	0.52	1.91
$\text{Sn}_2\text{InSe}_2\text{Cl}_3$	<i>Cmcm</i>	4.13	14.94	14.90	-718	0.66	0.60	0.68	0.35	1.82
	<i>Cmc21</i>	4.08	14.09	16.02	-767	1.05	-/-	1.68	1.58	1.35
	<i>P2₁/c</i>	6.35	16.79	8.09	-765	2.08	1.93	2.09	0.74	1.87
$\text{Sn}_2\text{InSe}_2\text{Br}_3$	<i>Cmcm</i>	4.42	14.54	15.01	-651	1.11	-/-	1.48	0.54	1.62
	<i>Cmc21</i>	3.98	15.22	15.58	-699	1.37	1.34	1.40	0.88	0.75
	<i>P2₁/c</i>	6.41	17.09	8.23	-688	1.84	1.49	1.86	1.02	0.60
$\text{Sn}_2\text{InSe}_2\text{I}_3$	<i>Cmcm</i>	4.39	15.73	15.31	-534	1.37	1.30	1.40	2.08	1.03
	<i>Cmc21</i>	4.32	15.93	16.32	-577	0.68	-/-	1.28	0.35	0.46
	<i>P2₁/c</i>	7.41	17.62	8.50	-567	1.95	1.79	1.96	0.50	0.79
$\text{Sn}_2\text{InTe}_2\text{Cl}_3$	<i>Cmcm</i>	4.19	12.25	18.40	-542	0.56	0.46	0.65	0.21	2.21
	<i>Cmc21</i>	4.16	13.24	17.21	-639	0.92	0.80	1.01	2.23	1.21
	<i>P2₁/c</i>	6.53	17.82	8.58	-610	1.59	-/-	1.71	1.45	1.50
$\text{Sn}_2\text{InTe}_2\text{Br}_3$	<i>Cmcm</i>	4.28	12.34	18.41	-488	-/-	-/-	0.65	-/-	-/-
	<i>Cmc21</i>	4.31	14.70	16.90	-559	0.53	-/-	0.79	0.83	0.96
	<i>P2₁/c</i>	6.48	18.04	8.60	-543	1.46	-/-	1.59	1.39	1.25
$\text{Sn}_2\text{InTe}_2\text{I}_3$	<i>Cmcm</i>	4.56	15.6	16.26	-425	1.09	0.99	1.13	1.50	0.64
	<i>Cmc21</i>	4.30	15.34	16.92	-460	0.87	0.80	0.96	0.79	0.49
	<i>P2₁/c</i>	6.58	18.87	8.74	-438	1.11	1.08	1.20	1.23	0.91
$\text{Sn}_2\text{SbS}_2\text{Cl}_3$	<i>Cmcm</i>	4.08	12.63	15.88	-649	1.68	1.61	1.77	1.03	1.24
	<i>Cmc21</i>	4.01	13.81	16.02	-655	1.24	1.06	1.29	0.39	2.82
	<i>P2₁/c</i>	6.96	16.05	8.08	-702	2.45	2.17	2.48	2.63	0.83
$\text{Sn}_2\text{SbS}_2\text{Br}_3$	<i>Cmcm</i>	4.10	13.47	15.40	-574	1.47	0.88	1.53	0.49	1.15
	<i>Cmc21</i>	4.10	13.92	16.12	-592	1.25	1.06	1.34	0.28	1.33
	<i>P2₁/c</i>	7.01	16.06	8.19	-646	2.19	1.99	2.29	2.31	0.78
$\text{Sn}_2\text{SbS}_2\text{I}_3$	<i>Cmcm</i>	4.24	13.84	15.76	-486	1.00	0.95	1.55	0.28	1.11
	<i>Cmc21</i>	4.26	14.22	16.24	-497	1.01	-/-	1.51	0.26	1.23
	<i>P2₁/c</i>	7.25	16.24	8.47	-555	1.76	1.69	1.77	0.60	0.58
	Exp. ^a	4.25	13.99	16.38	-/-	-/-	-/-	1.41	-/-	-/-
$\text{Sn}_2\text{SbSe}_2\text{Cl}_3$	<i>Cmcm</i>	4.16	12.48	16.92	-646	1.41	-/-	1.82	0.78	1.06
	<i>Cmc21</i>	4.07	14.01	16.45	-651	1.00	-/-	1.26	1.39	1.51
	<i>P2₁/c</i>	7.06	17.98	8.06	-692	2.18	1.84	2.20	2.38	2.06

System	Group	lat. parameters			E_{form} /eV	Atom $^{-1}$	$E_{\text{g, dir.}}$ /eV	$E_{\text{g, ind.}}$ /eV	$E_{\text{g, opt.}}$ /eV	eff. masses	
		a /Å	b /Å	c /Å						m_e^*/m_0	m_h^*/m_0
$\text{Sn}_2\text{SbSe}_2\text{Br}_3$	<i>Cmcm</i>	4.13	12.94	17.75	-572		1.41	1.33	1.50	1.32	1.68
	<i>Cmc21</i>	4.16	14.22	16.73	-586		0.94	0.89	1.04	0.29	1.50
	<i>P2₁/c</i>	7.10	17.16	8.29	-631		2.03	1.64	2.10	1.64	2.03
$\text{Sn}_2\text{SbSe}_2\text{I}_3$	<i>Cmcm</i>	4.28	13.95	16.44	-473		1.06	0.80	1.06	0.40	1.61
	<i>Cmc21</i>	4.31	14.50	16.91	-493		0.96	-/-	1.64	0.26	0.98
	<i>P2₁/c</i>	7.28	17.08	8.57	-547		1.89	1.67	1.98	0.82	1.31
	Exp. ^b	4.30	14.09	17.22	-/-		-/-	-/-	-/-	-/-	-/-
$\text{Sn}_2\text{SbTe}_2\text{Cl}_3$	<i>Cmcm</i>	4.34	12.40	17.68	-530		0.94	0.87	1.00	1.02	0.32
	<i>Cmc21</i>	4.34	12.39	17.70	-523		0.95	-/-	1.37	1.44	2.88
	<i>P2₁/c</i>	6.45	18.10	8.36	-588		0.56	0.48	0.65	0.47	1.99
$\text{Sn}_2\text{SbTe}_2\text{Br}_3$	<i>Cmcm</i>	4.24	12.51	19.69	-456		0.70	0.49	0.76	0.43	0.69
	<i>Cmc21</i>	4.27	14.66	17.39	-456		1.03	0.98	1.06	0.78	1.45
	<i>P2₁/c</i>	6.59	18.50	8.42	-518		0.55	0.25	0.57	0.67	1.13
$\text{Sn}_2\text{SbTe}_2\text{I}_3$	<i>Cmcm</i>	4.34	13.57	19.47	-352		0.79	0.47	0.80	0.58	0.99
	<i>Cmc21</i>	4.28	14.31	18.73	-358		0.38	0.19	0.44	0.56	0.34
	<i>P2₁/c</i>	7.02	18.82	8.67	-412		0.85	0.02	1.26	0.52	1.10
$\text{Sn}_2\text{BiS}_2\text{Cl}_3$	<i>Cmcm</i>	3.99	13.91	16.02	-714		1.54	0.99	1.55	0.61	0.63
	<i>Cmc21</i>	4.07	13.72	15.98	-716		1.15	1.03	1.17	0.26	2.25
	<i>P2₁/c</i>	6.97	15.93	8.10	-732		2.19	1.84	2.19	4.60	1.80
$\text{Sn}_2\text{BiS}_2\text{Br}_3$	<i>Cmcm</i>	4.11	13.42	15.68	-650		1.34	0.96	1.44	0.59	1.07
	<i>Cmc21</i>	4.11	13.42	15.68	-651		1.41	1.12	1.50	0.27	1.37
	<i>P2₁/c</i>	7.03	16.04	8.23	-675		1.97	1.72	2.07	3.90	1.41
$\text{Sn}_2\text{BiS}_2\text{I}_3$	<i>Cmcm</i>	4.26	13.92	15.93	-552		0.99	-/-	1.39	0.41	1.47
	<i>Cmc21</i>	4.26	13.92	15.94	-553		1.01	-/-	1.42	0.21	1.46
	<i>P2₁/c</i>	7.30	16.23	8.52	-583		1.61	1.49	1.60	0.66	0.56
	Exp. ^c	4.29	14.12	16.41	-/-		-/-	-/-	1.22	-/-	-/-
$\text{Sn}_2\text{BiSe}_2\text{Cl}_3$	<i>Cmcm</i>	4.03	12.5	17.07	-713		1.10	1.10	1.12	0.53	1.18
	<i>Cmc21</i>	4.13	13.98	16.46	-708		0.90	0.71	0.95	2.32	1.33
	<i>P2₁/c</i>	6.41	17.23	8.22	-731		1.20	1.08	1.25	0.3	1.72
$\text{Sn}_2\text{BiSe}_2\text{Br}_3$	<i>Cmcm</i>	4.13	13.02	17.29	-635		0.97	0.67	1.06	0.44	0.42
	<i>Cmc21</i>	4.21	14.14	16.74	-642		0.84	0.83	0.85	1.31	1.15
	<i>P2₁/c</i>	6.9	17.19	8.33	-662		1.43	1.12	1.45	0.74	1.93
$\text{Sn}_2\text{BiSe}_2\text{I}_3$	<i>Cmcm</i>	4.31	13.99	16.62	-538		1.05	0.77	1.14	0.26	0.31
	<i>Cmc21</i>	4.35	14.47	16.87	-538		1.06	0.88	1.16	0.64	0.94
	<i>P2₁/c</i>	7.33	17.08	8.60	-575		1.66	1.47	1.75	2.23	1.94
$\text{Sn}_2\text{BiTe}_2\text{Cl}_3$	<i>Cmcm</i>	4.15	12.37	17.83	-580		0.74	-/-	1.08	1.75	1.31
	<i>Cmc21</i>	4.2	12.37	17.84	-579		0.76	0.70	0.86	0.90	0.45
	<i>P2₁/c</i>	6.53	18.02	8.48	-612		0.50	0.48	0.58	0.36	0.64
$\text{Sn}_2\text{BiTe}_2\text{Br}_3$	<i>Cmcm</i>	4.24	12.63	18.26	-510		0.85	0.72	0.85	1.19	1.01
	<i>Cmc21</i>	4.24	12.63	18.26	-510		0.85	0.72	0.86	0.90	1.01
	<i>P2₁/c</i>	6.68	18.39	8.53	-542		0.60	0.44	0.69	0.29	1.23
$\text{Sn}_2\text{BiTe}_2\text{I}_3$	<i>Cmcm</i>	4.38	13.30	18.73	-399		-/-	-/-	0.77	-/-	-/-
	<i>Cmc21</i>	4.44	14.90	17.96	-407		0.61	0.58	0.69	0.32	1.49
	<i>P2₁/c</i>	7.12	18.67	8.75	-439		0.89	0.26	0.93	0.19	1.55
$\text{Pb}_2\text{InS}_2\text{Cl}_3$	<i>Cmcm</i>	4.06	15.04	14.60	-790		2.58	2.52	2.68	2.98	2.13
	<i>Cmc21</i>	4.10	15.02	15.44	-853		2.32	-/-	2.68	1.83	1.22
	<i>P2₁/c</i>	6.98	16.05	8.18	-810		3.03	2.91	2.94	1.21	2.65
$\text{Pb}_2\text{InS}_2\text{Br}_3$	<i>Cmcm</i>	4.17	15.31	14.73	-714		2.39	-/-	2.64	1.48	1.76
	<i>Cmc21</i>	4.20	15.83	15.52	-772		2.16	-/-	2.48	0.89	1.28
	<i>P2₁/c</i>	7.36	16.03	8.36	-736		2.94	2.76	2.81	1.39	2.50
$\text{Pb}_2\text{InS}_2\text{I}_3$	<i>Cmcm</i>	4.38	16.02	15.03	-588		1.84	-/-	2.29	0.27	1.48
	<i>Cmc21</i>	4.35	16.90	15.47	-644		1.93	-/-	2.14	0.53	1.83
	<i>P2₁/c</i>	7.74	16.41	8.61	-626		2.53	2.50	2.59	2.02	1.05

System	Group	lat. parameters			E_{form} /eV Atom $^{-1}$	$E_{\text{g, dir.}}$ /eV	$E_{\text{g, ind.}}$ /eV	$E_{\text{g, opt.}}$ /eV	eff. masses	
		a /Å	b /Å	c /Å					m_{e}^*/m_0	m_{h}^*/m_0
$\text{Pb}_2\text{InSe}_2\text{Cl}_3$	$Cmcm$	4.05	15.38	15.20	-795	2.03	1.91	2.06	0.72	1.53
	$Cmc2_1$	4.16	14.66	16.02	-846	1.77	1.73	1.85	1.30	1.03
	$P2_1/c$	6.47	16.78	8.42	-825	2.55	2.39	2.59	1.85	2.72
$\text{Pb}_2\text{InSe}_2\text{Br}_3$	$Cmcm$	4.16	15.59	15.31	-715	1.96	1.87	2.05	1.65	0.84
	$Cmc2_1$	4.25	15.61	16.12	-767	1.71	-/-	2.18	0.85	1.14
	$P2_1/c$	7.47	16.45	8.48	-777	2.09	2.01	2.11	0.79	1.66
$\text{Pb}_2\text{InSe}_2\text{I}_3$	$Cmcm$	4.36	16.1	15.51	-606	1.72	-/-	1.93	2.31	0.76
	$Cmc2_1$	4.40	16.62	16.25	-647	1.56	-/-	1.88	0.45	1.38
	$P2_1/c$	7.89	16.67	8.79	-659	1.70	-/-	2.20	0.61	1.66
$\text{Pb}_2\text{InTe}_2\text{Cl}_3$	$Cmcm$	4.27	15.46	16.15	-661	1.03	1.00	0.97	0.62	2.27
	$Cmc2_1$	4.23	13.25	17.42	-718	1.14	1.08	1.18	1.3	0.51
	$P2_1/c$	8.61	14.61	8.54	-726	1.66	1.59	1.74	1.15	0.40
$\text{Pb}_2\text{InTe}_2\text{Br}_3$	$Cmcm$	4.32	15.72	16.30	-600	1.15	1.05	1.07	0.59	1.28
	$Cmc2_1$	4.28	14.28	17.33	-643	1.27	1.22	1.36	1.91	0.77
	$P2_1/c$	7.41	17.54	8.46	-644	1.76	1.73	1.74	0.75	0.31
$\text{Pb}_2\text{InTe}_2\text{I}_3$	$Cmcm$	4.42	16.38	16.46	-488	1.23	1.06	1.32	0.58	1.24
	$Cmc2_1$	4.38	15.23	17.26	-528	1.15	-/-	1.33	1.06	1.42
	$P2_1/c$	7.78	17.77	8.78	-536	1.34	1.27	1.30	0.44	0.51
$\text{Pb}_2\text{SbS}_2\text{Cl}_3$	$Cmcm$	5.37	13.9	13.52	-667	2.03	-/-	2.06	2.14	1.91
	$Cmc2_1$	4.17	13.88	16.66	-704	1.87	1.79	1.97	0.77	2.34
	$P2_1/c$	6.70	15.76	8.29	-776	2.78	2.50	2.69	3.76	4.47
$\text{Pb}_2\text{SbS}_2\text{Br}_3$	$Cmcm$	4.18	14.51	16.25	-609	1.83	1.65	1.88	1.38	1.11
	$Cmc2_1$	4.18	14.51	16.26	-634	1.54	-/-	1.73	0.41	1.39
	$P2_1/c$	7.03	15.92	8.38	-721	2.55	2.41	2.60	1.89	3.96
$\text{Pb}_2\text{SbS}_2\text{I}_3$	$Cmcm$	4.32	14.06	15.82	-517	1.27	-/-	1.78	0.37	0.62
	$Cmc2_1$	4.32	14.88	16.44	-536	1.37	-/-	1.86	0.25	1.06
	$P2_1/c$	7.36	16.30	8.59	-624	2.12	2.09	2.21	0.63	1.14
	Exp. ^d	4.33	14.18	16.56	-/-	-/-	-/-	2.00	-/-	-/-
	Exp. ^e	7.36	16.47	8.59	-/-	-/-	-/-	-/-	-/-	-/-
$\text{Pb}_2\text{SbSe}_2\text{Cl}_3$	$Cmcm$	5.81	14.29	13.36	-643	1.46	-/-	1.61	0.69	2.37
	$Cmc2_1$	4.24	13.42	17.33	-706	1.38	1.31	1.47	0.75	2.64
	$P2_1/c$	7.15	18.13	8.16	-761	2.42	2.19	2.43	1.18	2.10
$\text{Pb}_2\text{SbSe}_2\text{Br}_3$	$Cmcm$	4.23	14.29	17.5	-595	1.58	1.28	1.67	0.79	2.73
	$Cmc2_1$	4.24	14.43	17.49	-636	1.47	1.28	1.56	0.83	1.30
	$P2_1/c$	7.17	16.91	8.44	-702	2.17	1.88	2.25	2.03	2.22
$\text{Pb}_2\text{SbSe}_2\text{I}_3$	$Cmcm$	4.36	14.15	16.44	-507	1.19	1.14	1.30	0.46	1.36
	$Cmc2_1$	4.35	15.44	17.56	-547	1.10	-/-	1.40	0.73	0.88
	$P2_1/c$	7.37	16.99	8.73	-615	1.98	1.92	2.07	2.76	2.29
$\text{Pb}_2\text{SbTe}_2\text{Cl}_3$	$Cmcm$	5.21	13.8	15.60	-595	1.77	1.64	1.73	0.53	0.92
	$Cmc2_1$	4.36	12.98	18.71	-569	0.75	-/-	0.91	1.17	2.39
	$P2_1/c$	6.36	18.48	8.37	-648	0.93	0.90	1.01	0.46	1.18
$\text{Pb}_2\text{SbTe}_2\text{Br}_3$	$Cmcm$	4.55	12.69	17.93	-508	0.77	-/-	1.67	0.25	0.96
	$Cmc2_1$	4.26	13.24	19.08	-510	0.79	0.70	0.89	0.89	1.61
	$P2_1/c$	6.59	18.76	8.55	-577	0.85	0.72	0.91	0.46	0.92
$\text{Pb}_2\text{SbTe}_2\text{I}_3$	$Cmcm$	4.38	13.79	19.31	-355	0.85	0.55	0.96	0.16	0.93
	$Cmc2_1$	4.35	14.33	19.03	-419	0.93	0.83	1.02	0.77	1.34
	$P2_1/c$	7.22	18.75	8.83	-471	0.90	0.37	0.85	0.13	0.86
$\text{Pb}_2\text{BiS}_2\text{Cl}_3$	$Cmcm$	4.11	12.83	15.79	-748	1.92	1.64	1.91	0.76	3.04
	$Cmc2_1$	4.18	13.77	16.68	-773	1.72	1.60	1.68	1.39	3.75
	$P2_1/c$	6.97	15.81	8.30	-793	2.61	2.40	2.58	5.44	1.54
$\text{Pb}_2\text{BiS}_2\text{Br}_3$	$Cmcm$	4.22	13.53	15.63	-682	1.76	1.52	1.85	0.61	1.47
	$Cmc2_1$	4.25	14.66	16.92	-700	1.66	1.47	1.56	1.04	1.55
	$P2_1/c$	7.11	16.02	8.41	-740	2.284	2.28	2.38	1.86	0.97

System	Group	lat. parameters			E_{form} /eV Atom $^{-1}$	$E_{\text{g, dir.}}$ /eV	$E_{\text{g, ind.}}$ /eV	$E_{\text{g, opt.}}$ /eV	eff. masses	
		a /Å	b /Å	c /Å					m_{e}^*/m_0	m_{h}^*/m_0
$\text{Pb}_2\text{BiS}_2\text{I}_3$	$Cmcm$	4.33	14.1	16.03	-582	1.29	-/-	1.68	0.44	0.60
	$Cmc2_1$	4.33	14.12	16.05	-581	1.30	-/-	1.71	0.45	0.61
	$P2_1/c$	7.43	16.32	8.63	-645	1.92	-/-	2.26	0.65	1.07
	$Exp.^f$	4.32	14.26	15.49	-/-	-/-	-/-	1.60	-/-	-/-
$\text{Pb}_2\text{BiSe}_2\text{Cl}_3$	$Cmcm$	4.21	13.16	16.88	-728	1.81	1.74	1.78	1.12	1.80
	$Cmc2_1$	4.22	13.46	17.34	-773	1.27	1.19	1.26	0.85	1.70
	$P2_1/c$	7.22	18.63	8.17	-786	2.36	2.19	2.36	2.48	1.97
$\text{Pb}_2\text{BiSe}_2\text{Br}_3$	$Cmcm$	4.28	14.34	17.61	-667	1.37	1.14	1.42	0.58	1.34
	$Cmc2_1$	4.29	14.4	17.59	-703	1.20	1.07	1.26	0.45	1.10
	$P2_1/c$	7.23	16.96	8.50	-722	1.96	1.84	1.95	2.63	0.89
$\text{Pb}_2\text{BiSe}_2\text{I}_3$	$Cmcm$	4.38	14.15	16.64	-572	1.17	1.09	1.26	0.50	1.17
	$Cmc2_1$	4.40	15.46	17.69	-600	1.07	-/-	1.26	0.38	0.82
	$P2_1/c$	7.45	17.04	8.76	-637	1.71	-/-	2.04	2.01	0.66
$\text{Pb}_2\text{BiTe}_2\text{Cl}_3$	$Cmcm$	4.33	12.46	17.78	-640	0.63	-/-	1.17	0.83	2.28
	$Cmc2_1$	4.29	12.96	18.93	-629	0.40	0.39	0.45	0.99	0.98
	$P2_1/c$	6.36	18.47	8.45	-682	1.09	1.09	1.19	0.43	0.88
$\text{Pb}_2\text{BiTe}_2\text{Br}_3$	$Cmcm$	4.34	12.65	18.28	-523	0.92	-/-	1.12	0.89	2.50
	$Cmc2_1$	4.30	13.40	19.06	-561	0.78	0.69	0.87	1.32	1.19
	$P2_1/c$	6.51	19.17	8.61	-604	1.21	1.12	1.15	2.21	1.21
$\text{Pb}_2\text{BiTe}_2\text{I}_3$	$Cmcm$	4.46	13.94	18.75	-419	0.74	0.54	0.83	0.63	0.83
	$Cmc2_1$	4.48	15.3	18.79	-465	0.55	0.44	0.53	2.52	1.05
	$P2_1/c$	7.23	18.83	8.90	-494	0.98	0.50	1.05	0.84	1.38

^a Lat. para. are taken from RT ($T = 293\text{ K}$) XRD meas. using Mo $K\alpha$ radiation[24] and band gap are taken from UV/vis absorption meas.[16]

^b Lat. para. are taken from low-temp. ($T = 173\text{ K}$) XRD meas. using Mo $K\alpha$ radiation.[24]

^c Lat. para. are taken from RT ($T = 293\text{ K}$) XRD meas. using Mo $K\alpha$ radiation and band gap are taken from UV/vis absorption meas.[25]

^d Lat. para. for $Cmcm$ are taken from RT ($T = 293\text{ K}$) XRD meas. using Mo $K\alpha$ radiation[27] and band gap are taken photoconductivity meas.[88]

^e Lat. para. for $P2_1/c$ are taken from low-temp. ($T = 100\text{ K}$) XRD meas. using Mo $K\alpha$ radiation.[27]

^f Lat. para. are taken from RT ($T = 293\text{ K}$) XRD meas. using Mo $K\alpha$ radiation and band gap are taken from UV/vis absorption meas.[25]

SM6: RANDOM FOREST REGRESSION RESULTS FOR PREDICTING THE FORMATION ENERGIES IN $Cmc2_1$ AND $P2_1/c$

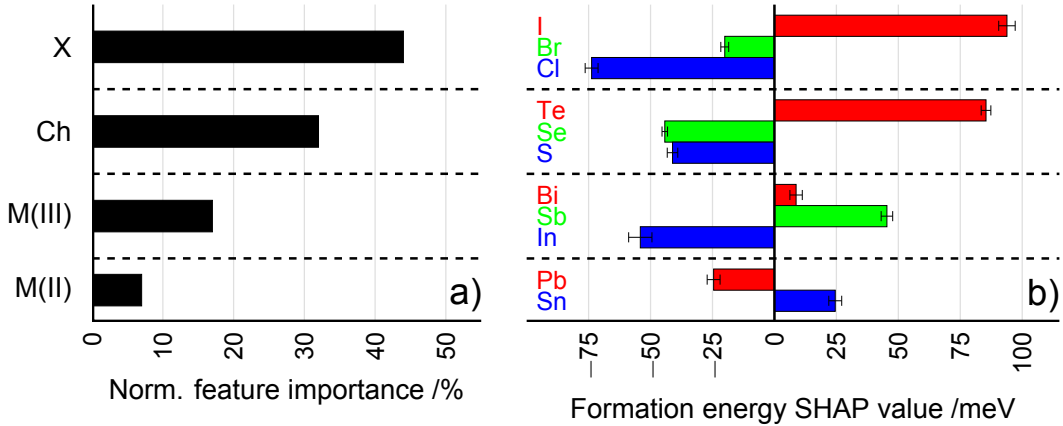


Figure 4. Summary of the feature importance for the formation energy RF model in $Cmc2_1$ MMCH compounds. a) Normalised atom site importance on the predicted formation energies in percent. b) Impact of elements within the M(II)-, M(III)-, Ch- and X-sites measured as mean shapley additive explanations (SAHP) values on the predicted base formation energy value in meV. The standard deviation for each mean SHAP value is displayed as error bars.

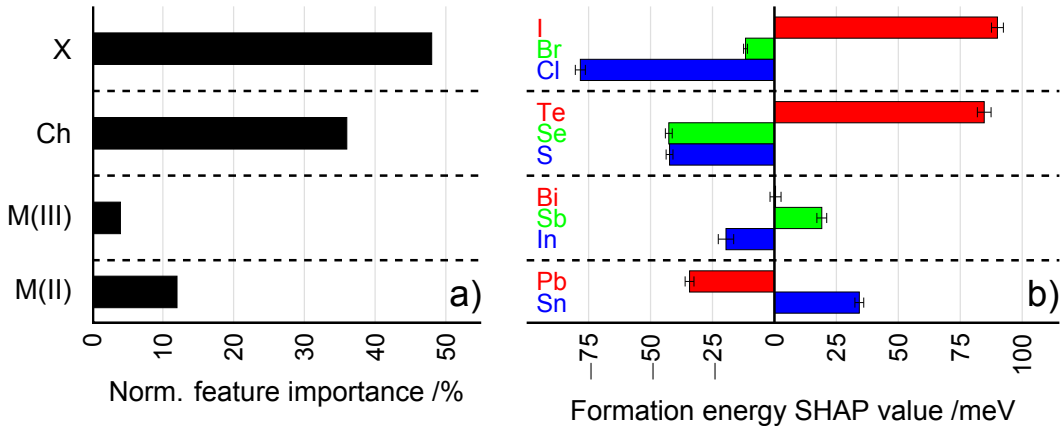


Figure 5. Summary of the feature importance for the formation energy RF model in $P2_1/c$ MMCH compounds. a) Normalised atom site importance on the predicted formation energies in percent. b) Impact of elements within the M(II)-, M(III)-, Ch- and X-sites measured as mean SAHP values on the predicted base formation energy value in meV. The standard deviation for each mean SHAP value is displayed as error bars.

Note that the formation energy in Figures 4 and 5 is negative, meaning that negative mean SHAP values indicate an increase in formation energy, whereas positive mean SHAP values indicate a decrease.

SM7: RANDOM FOREST REGRESSION RESULTS FOR PREDICTING THE FUNDAMENTAL BAND GAPS IN $Cmc2_1$ AND $P2_1/c$

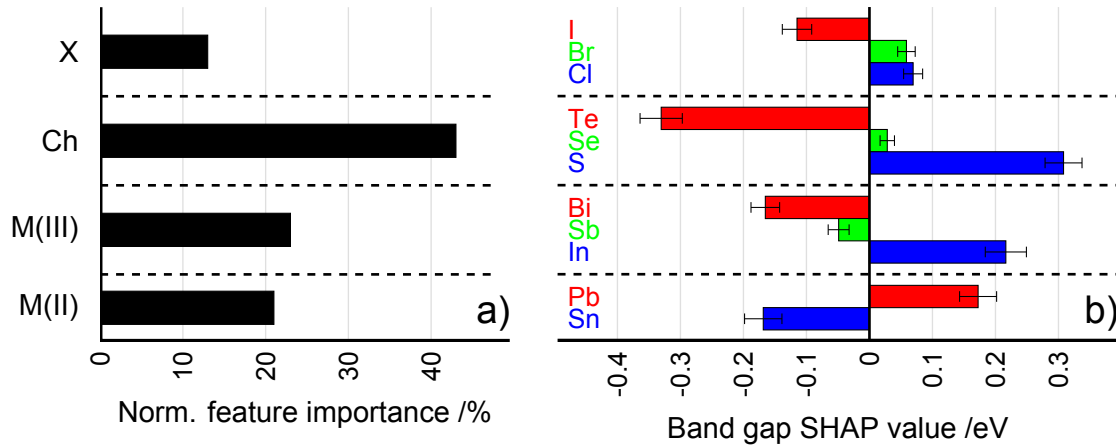


Figure 6. Summary of the feature importance for the fundamental band gap RF model in $Cmc2_1$ MMCH compounds. a) Normalised atom site importance on the predicted fundamental band gaps in percent. b) Impact of elements within the M(II)-, M(III)-, Ch- and X-sites measured as mean SAHP values on the predicted base fundamental band gap value in eV. The standard deviation for each mean SHAP value is displayed as error bars.

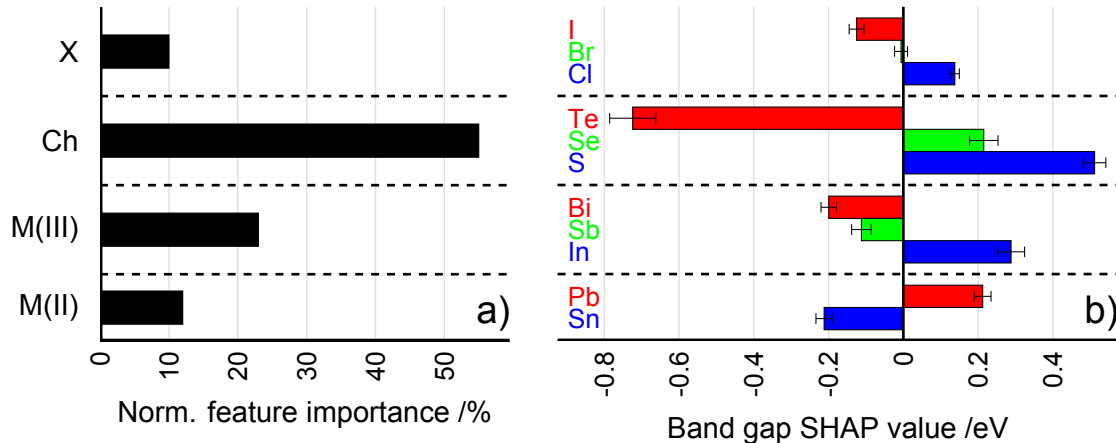


Figure 7. Summary of the feature importance for the fundamental band gap RF model in $P2_1/c$ MMCH compounds. a) Normalised atom site importance on the predicted fundamental band gaps in percent. b) Impact of elements within the M(II)-, M(III)-, Ch- and X-sites measured as mean SAHP values on the predicted base fundamental band gap value in eV. The standard deviation for each mean SHAP value is displayed as error bars.

SM8: RANDOM FOREST REGRESSION RESULTS FOR PREDICTING THE LOWEST DIRECT BAND GAPS IN *Cmcm*, *Cmc2*₁ AND *P2*₁/*c*

In analogy to the discussion of the fundamental band gap in the main text [see Section 3.2], we determined the direct band gaps of all Perovskite-inspired quaternary mixed-metal chalcohalides (MMCHs) per phase. In the case that the fundamental band gap is not a direct one, the lowest direct band gap between valence and conduction band has been determined for those indirect MMCH compounds. In contrast to indirect band gaps, direct band gaps do not require an additional phonon to perform the transition. However, these direct gaps require higher photon energies than the minimal indirect band gaps within the material in order to be overtaken. Nevertheless, such transitions are also of interest e.g. for photovoltaic applications, so we calculated them as well and the results are shown in the following SI Figures 8, 9 and 10 for *Cmcm*, *Cmc2*₁ and *P2*₁/*c*. Generally, we obtain analogous trends compared to the discussed fundamental band gaps in the main text, see Section 3.2 within the main text.

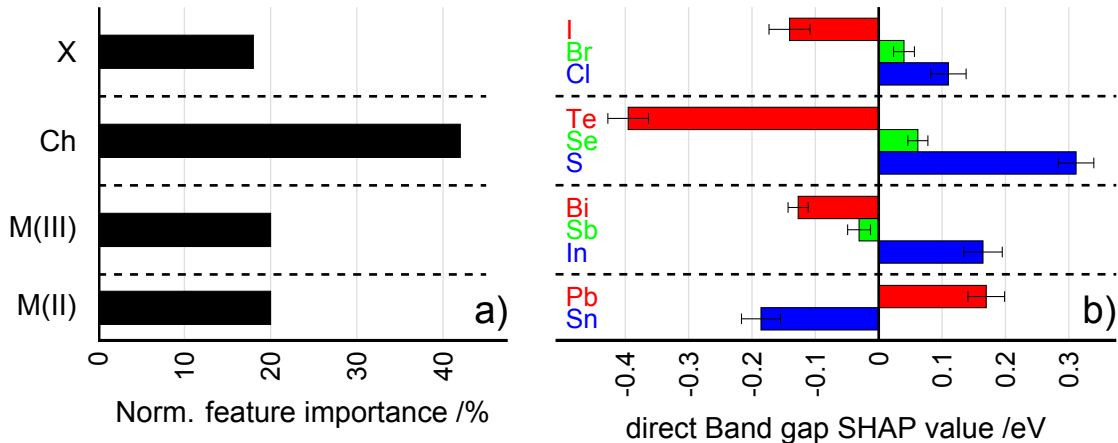


Figure 8. Summary of the feature importance for the lowest direct band gap RF model in *Cmcm* MMCH compounds. a) Normalised atom site importance on the predicted lowest direct band gaps in percent. b) Impact of elements within the M(II)-, M(III)-, Ch- and X-sites measured as mean SAHP values on the predicted base lowest direct band gap value in eV. The standard deviation for each mean SHAP value is displayed as error bars.

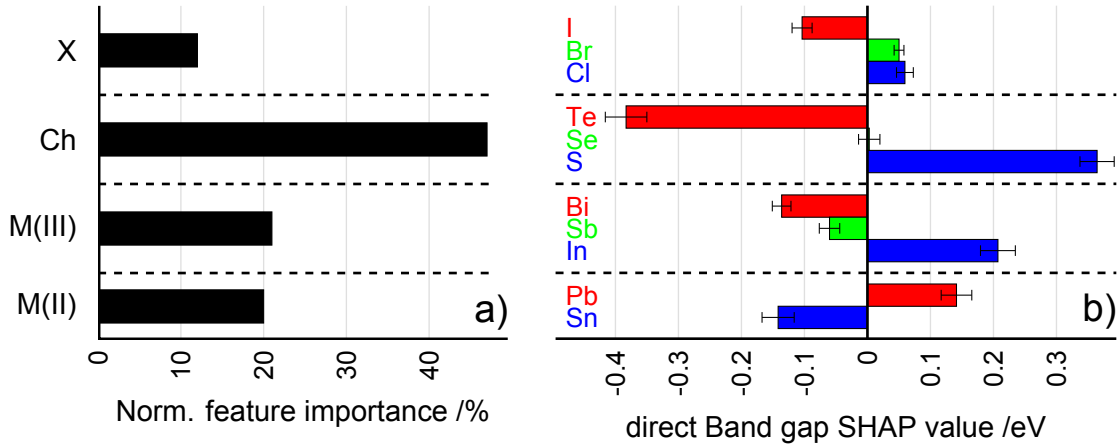


Figure 9. Summary of the feature importance for the lowest direct band gap RF model in $Cmc2_1$ MMCH compounds. a) Normalised atom site importance on the predicted lowest direct band gaps in percent. b) Impact of elements within the M(II)-, M(III)-, Ch- and X-sites measured as mean SAHP values on the predicted base lowest direct band gap value in eV. The standard deviation for each mean SHAP value is displayed as error bars.

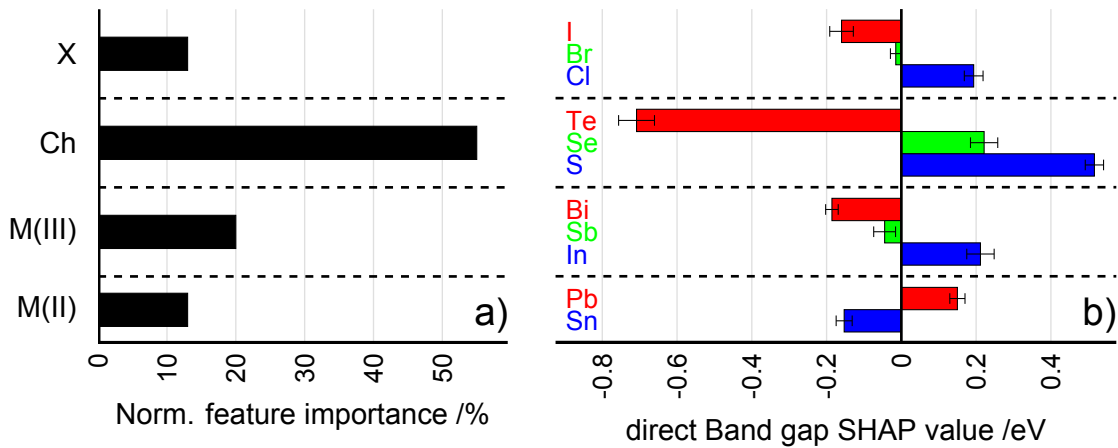


Figure 10. Summary of the feature importance for the lowest direct band gap RF model in $P2_1/c$ MMCH compounds. a) Normalised atom site importance on the predicted lowest direct band gaps in percent. b) Impact of elements within the M(II)-, M(III)-, Ch- and X-sites measured as mean SAHP values on the predicted base lowest direct band gap value in eV. The standard deviation for each mean SHAP value is displayed as error bars.

SM9: RANDOM FOREST REGRESSION RESULTS FOR PREDICTING THE OPTICAL BAND GAPS IN *Cmcm*, *Cmc2*₁ AND *P2*₁/*c*

Besides the fundamental band gaps [see main text Figure 3, as well as SI Figures in Sections S7 and S8] we determined the optical band gap by means of a Tauc plot based on the adsorption spectra of the respective MMCH material. Generally, there are two main findings for the optical band gaps. First, the optical band gaps are larger than the fundamental gaps, see SI table I. This is caused by i) a low density of states at the band edges resulting from a low electronic degeneracy due to the low crystal symmetry (for *Cmcm* and *Cmc2*₁) as well as ii) a weak transition dipole moment between the valence and the conduction band minimum due to the symmetry restrictions and a low spatial overlap.[17] Kavanagh *et al.* identified this mismatch between fundamental and optical band gap for Sn₂SbS₂I₃[17] and we confirmed this in our previous study for lead-free MMCHs.[20] Now, we observe this mismatch between fundamental and optical band gap for all 27 lead-free and 27 lead-based investigated MMCHs per phase, see discussion in Section 3.2 main text. This indicates that such a mismatch occurs for all compounds within the MMCH material space. Furthermore, we obtained analogue trends regarding the effect of atom sites and the elements on the optical band gap compared to the fundamental band gap, see discussion in Section 3.2 main text.

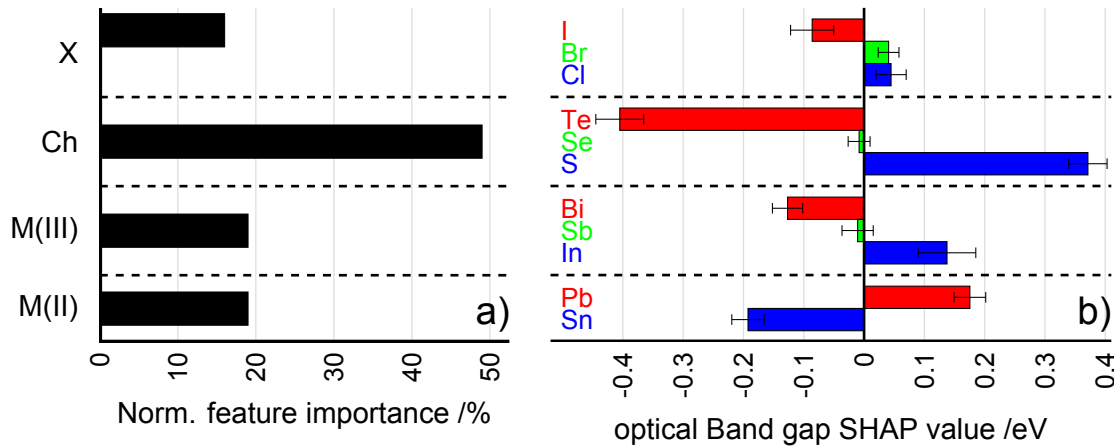


Figure 11. Summary of the feature importance for the optical band gap RF model in *Cmcm* MMCH compounds. a) Normalised atom site importance on the predicted optical band gaps in percent. b) Impact of elements within the M(II)-, M(III)-, Ch- and X-sites measured as mean SHAP values on the predicted base optical band gap value in eV. The standard deviation for each mean SHAP value is displayed as error bars.

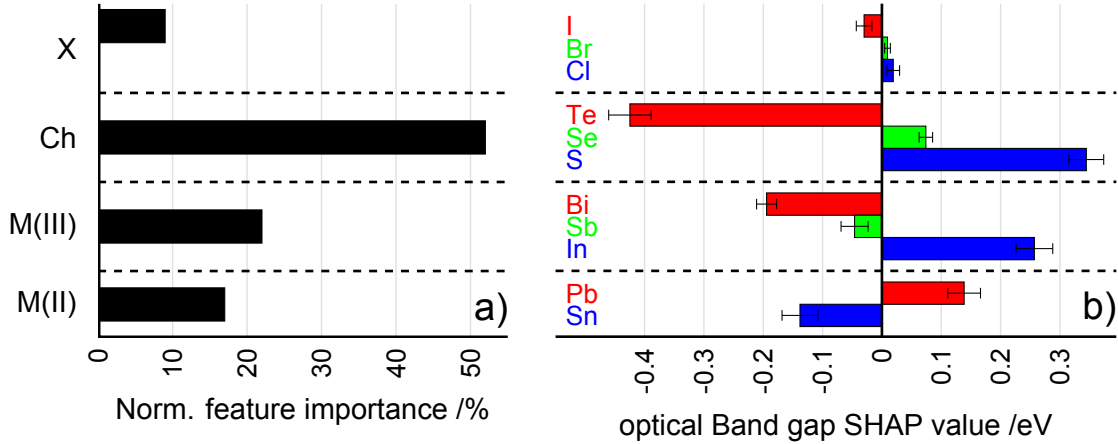


Figure 12. Summary of the feature importance for the optical band gap RF model in $Cmc2_1$ MMCH compounds. a) Normalised atom site importance on the predicted optical band gaps in percent. b) Impact of elements within the M(II)-, M(III)-, Ch- and X-sites measured as mean SAHP values on the predicted base optical band gap value in eV. The standard deviation for each mean SHAP value is displayed as error bars.

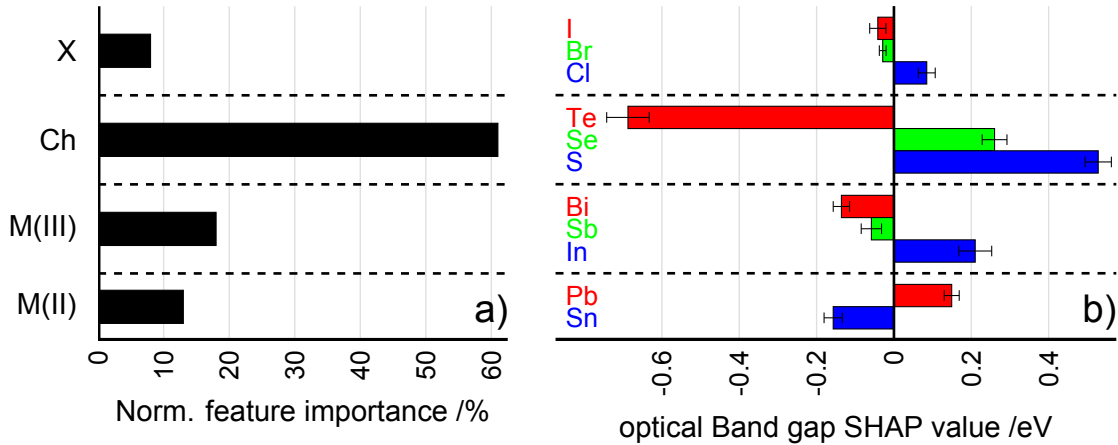


Figure 13. Summary of the feature importance for the optical band gap RF model in $P2_1/c$ MMCH compounds. a) Normalised atom site importance on the predicted optical band gaps in percent. b) Impact of elements within the M(II)-, M(III)-, Ch- and X-sites measured as mean SAHP values on the predicted base optical band gap value in eV. The standard deviation for each mean SHAP value is displayed as error bars.

SM10: RANDOM FOREST REGRESSION RESULTS FOR PREDICTING THE EFFECTIVE ELECTRON AND HOLE MASSES IN $Cmc2_1$ AND $P2_1/c$

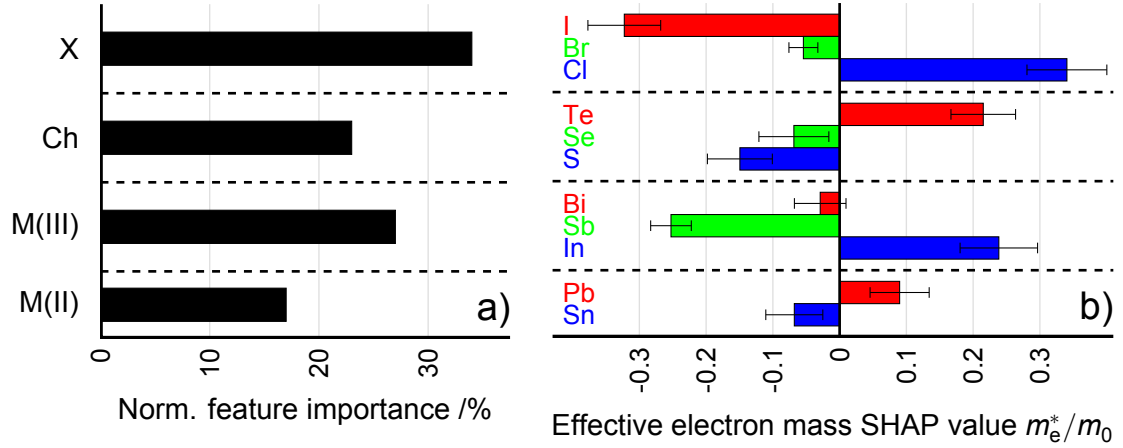


Figure 14. Summary of the feature importance for the effective electron mass RF model in $Cmc2_1$ MMCH compounds. a) Normalised atom site importance on the predicted effective electron masses in percent. b) Impact of elements within the M(II)-, M(III)-, Ch- and X-sites measured as mean SAHP values on the predicted base effective electron mass value per m_0 electron mass (9.109×10^{-31} kg). The standard deviation for each mean SHAP value is displayed as error bars.

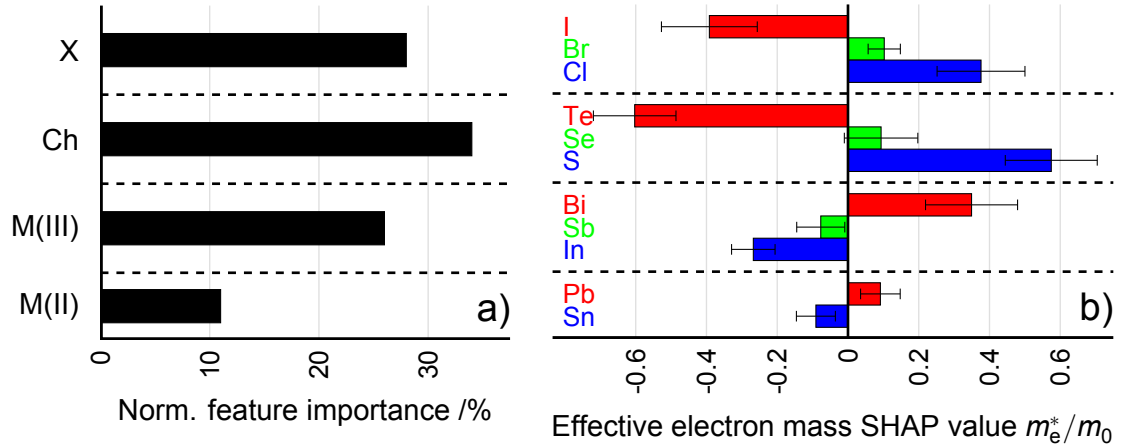


Figure 15. Summary of the feature importance for the effective electron mass RF model in $P2_1/c$ MMCH compounds. a) Normalised atom site importance on the predicted effective electron masses in percent. b) Impact of elements within the M(II)-, M(III)-, Ch- and X-sites measured as mean SAHP values on the predicted base effective electron mass value per m_0 electron mass (9.109×10^{-31} kg). The standard deviation for each mean SHAP value is displayed as error bars.

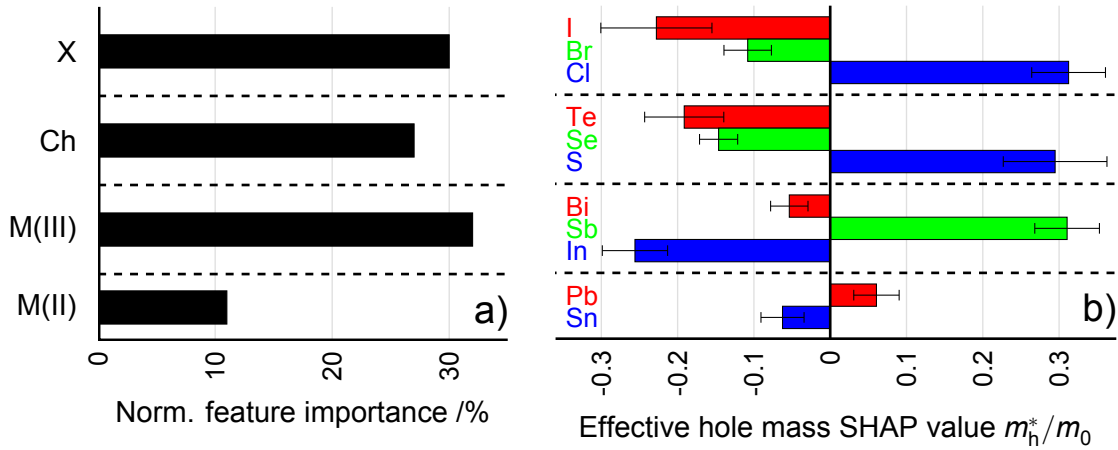


Figure 16. Summary of the feature importance for the effective hole mass RF model in *Cmc2₁* MMCH compounds. a) Normalised atom site importance on the predicted effective hole masses in percent. b) Impact of elements within the M(II)-, M(III)-, Ch- and X-sites measured as mean SAHP values on the predicted base effective hole mass value per m_0 electron mass (9.109×10^{-31} kg). The standard deviation for each mean SHAP value is displayed as error bars.

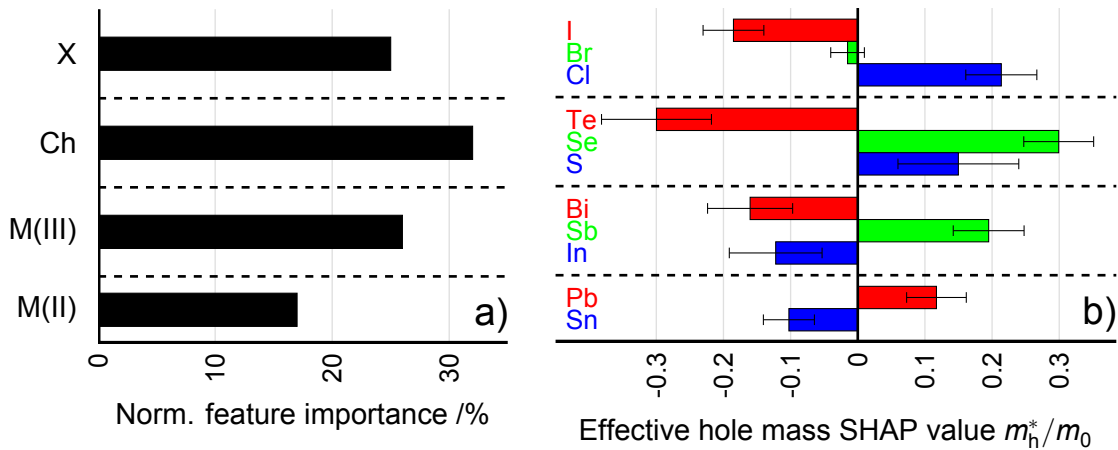


Figure 17. Summary of the feature importance for the effective hole mass RF model in *P2₁/c* MMCH compounds. a) Normalised atom site importance on the predicted effective hole masses in percent. b) Impact of elements within the M(II)-, M(III)-, Ch- and X-sites measured as mean SAHP values on the predicted base effective hole mass value per m_0 electron mass (9.109×10^{-31} kg). The standard deviation for each mean SHAP value is displayed as error bars.

SM11: DENSITY OF STATES OF LEAD-FREE AND LEAD-BASED
 $M(II)_2BiSe_2Br_3$ COMPOUNDS IN $Cmc2_1$ AND $P2_1/c$ PHASES

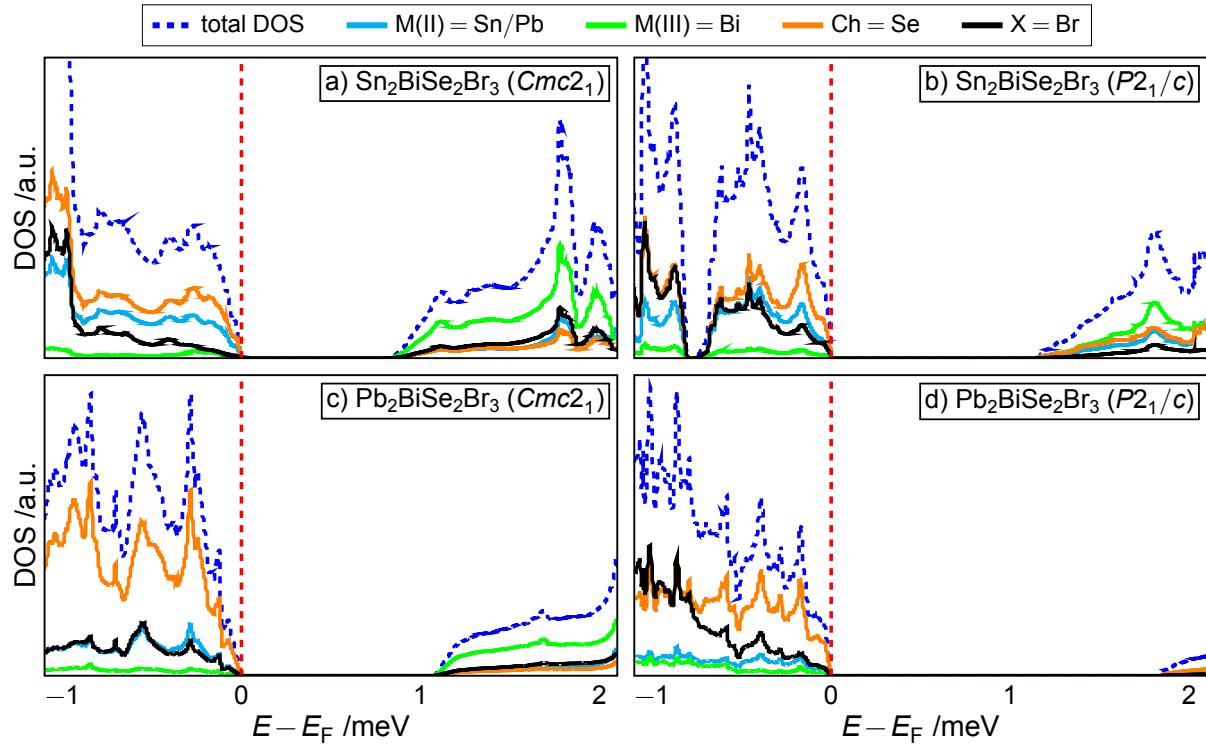


Figure 18. Density of state for $Sn_2BiSe_2Br_3$ at a) $Cmc2_1$ and b) $P2_1/c$ phases as well as for $Pb_2BiSe_2Br_3$ at c) $Cmc2_1$ and $P2_1/c$ phases.

SM12: BAND STRUCTURES OF LEAD-FREE AND LEAD-BASED
 $M(II)_2BiSe_2Br_3$ COMPOUNDS IN $Cmcm$, $Cmc2_1$ AND $P2_1/c$ PHASES

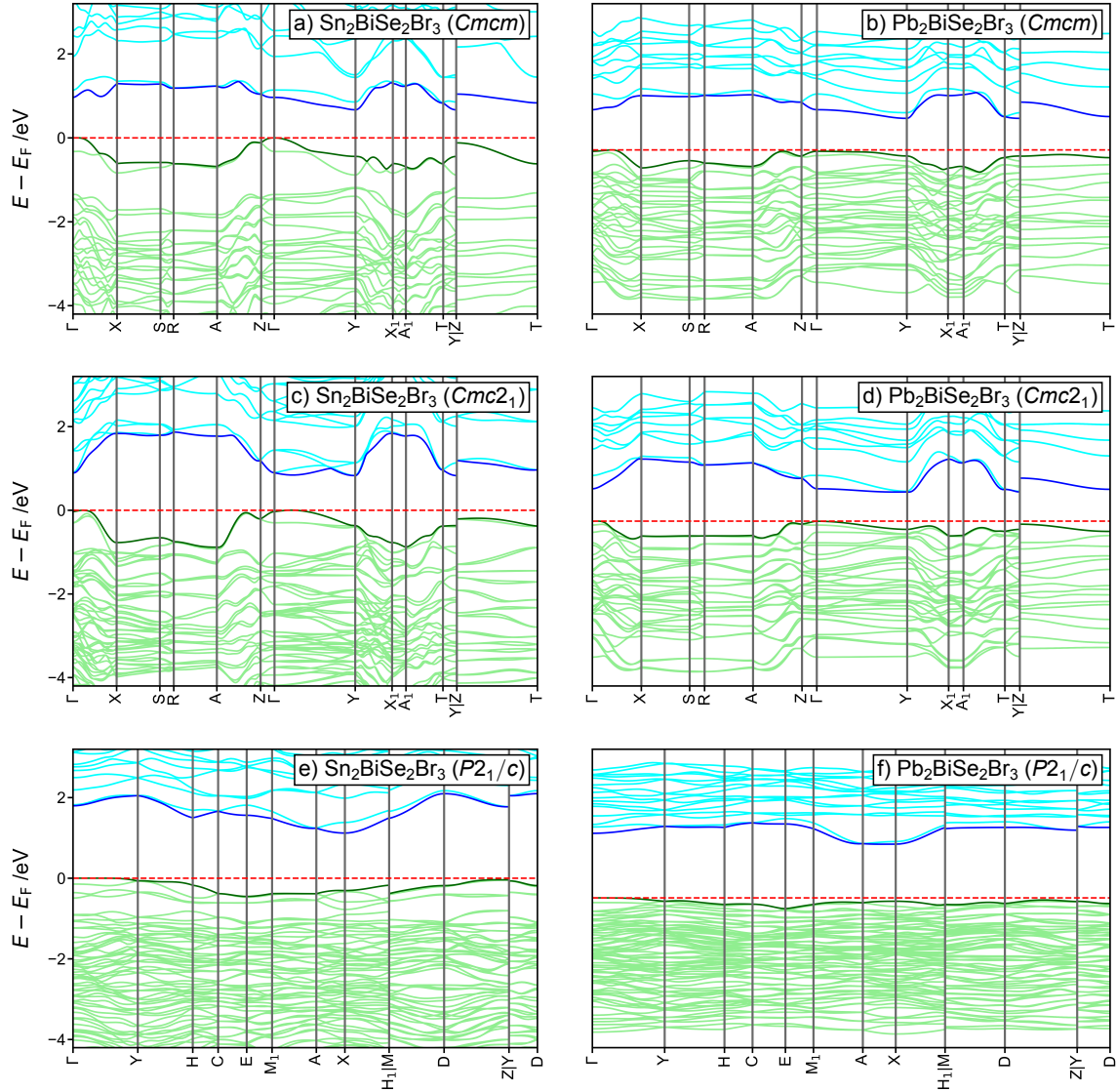


Figure 19. Band structures for $Sn_2BiSe_2Br_3$ at a) $Cmcm$, c) $Cmc2_1$ and e) $P2_1/c$ phases as well as for $Pb_2BiSe_2Br_3$ at b) $Cmcm$, d) $Cmc2_1$ and f) $P2_1/c$ phases. Colors: Light green denotes the valence bands, with the highest occupied band highlighted in dark green. Cyan denotes the conduction bands, with the lowest unoccupied band highlighted in blue.

SM13: COMPARISON OF MMCHs MATERIAL PROPERTIES IN $Cmc2_1$ AND $P2_1/c$

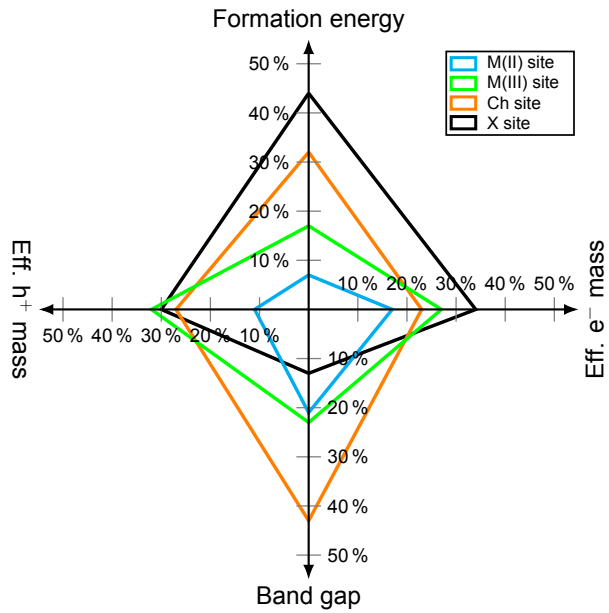


Figure 20. Summary of atom site importance on the formation energy, band gap, as well as the effective masses of electrons and holes in $Cmc2_1$.

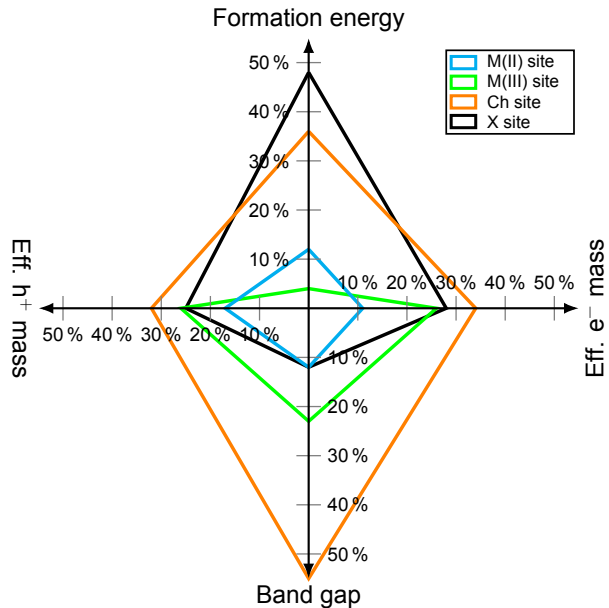


Figure 21. Summary of atom site importance on the formation energy, band gap, as well as the effective masses of electrons and holes in $P2_1/c$.